

Wind properties of variable B supergiants

Evidence of pulsations connected with mass-loss episodes^{*}

M. Haucke^{1,2}, L. S. Cidale^{1,2,3}, R. O. J. Venero^{1,2}, M. Curé³, M. Kraus^{4,5}, S. Kanaan³, and C. Arcos³

¹ Departamento de Espectroscopía, Facultad de Ciencias Astronómicas y Geofísicas, Universidad Nacional de La Plata, Paseo del Bosque S/N, La Plata, Argentina.

e-mail: mhaucke@fcaglp.unlp.edu.ar

² Instituto de Astrofísica de La Plata, CONICET-UNLP, Paseo del Bosque S/N, La Plata, Argentina.

³ Instituto de Física y Astronomía, Facultad de Ciencias, Universidad de Valparaíso, Av. Gran Bretaña 1111, Casilla 5030, Valparaíso, Chile.

⁴ Astronomický ústav, Akademie věd České republiky v.v.i., Fričova 298, 251 65, Ondřejov, Czech Republic.

⁵ Tartu Observatory, Tõravere, 61602 Tartumaa, Estonia.

Received date / Accepted date

ABSTRACT

Context. Variable B supergiants (BSGs) constitute a heterogeneous group of stars with complex photometric and spectroscopic behaviours. They exhibit mass-loss variations and experience different types of oscillation modes, and there is growing evidence that variable stellar winds and photospheric pulsations are closely related.

Aims. To discuss the wind properties and variability of evolved B-type stars, we derive new stellar and wind parameters for a sample of 19 Galactic BSGs by fitting theoretical line profiles of H, He, and Si to the observed ones and compare them with previous determinations.

Methods. The synthetic line profiles are computed with the non-local thermodynamic equilibrium (NLTE) atmosphere code FAST-WIND, with a β -law for hydrodynamics.

Results. The mass-loss rate of three stars has been obtained for the first time. The global properties of stellar winds of mid/late B supergiants are well represented by a β -law with $\beta > 2$. All stars follow the known empirical wind momentum–luminosity relationships, and the late BSGs show the trend of the mid BSGs. HD 75149 and HD 99953 display significant changes in the shape and intensity of the H α line (from a pure absorption to a P Cygni profile, and vice versa). These stars have mass-loss variations of almost a factor of 2.8. A comparison among mass-loss rates from the literature reveals discrepancies of a factor of 1 to 7. This large variation is a consequence of the uncertainties in the determination of the stellar radius. Therefore, for a reliable comparison of these values we used the invariant parameter Q_r . Based on this parameter, we find an empirical relationship that associates the amplitude of mass-loss variations with photometric/spectroscopic variability on timescales of tens of days. We find that stars located on the cool side of the bi-stability jump show a decrease in the ratio V_∞/V_{esc} , while their corresponding mass-loss rates are similar to or lower than the values found for stars on the hot side. Particularly, for those variable stars a decrease in V_∞/V_{esc} is accompanied by a decrease in \dot{M} .

Conclusions. Our results also suggest that radial pulsation modes with periods longer than 6 days might be responsible for the wind variability in the mid/late-type BSGs. These radial modes might be identified with strange modes, which are known to facilitate (enhanced) mass loss. On the other hand, we propose that the wind behaviour of stars on the cool side of the bi-stability jump could fit with predictions of the δ – *slow* hydrodynamics solution for radiation-driven winds with highly variable ionization.

Key words. stars: early-type – stars: supergiants – stars: mass-loss – stars: winds, outflows – stars: mass-loss.

1. Introduction

Massive stars have a significant impact on the ionization, structure, and evolution of the interstellar medium (ISM). Via their stellar winds they release energy and momentum to their surroundings leading to the formation of stellar wind-blown bubbles, bow-shocks, and circumstellar shells. On the other hand, the huge amount of mass lost from the stars modifies the later stages of their lives (evolutionary timescales and final core

masses) as well as the type of SN remnants left (Meynet et al. 1994; Woosley et al. 2002).

Stellar winds of hot massive stars are mainly driven by line scattering of UV photons coming from the stars' continuum radiation. The standard stationary radiation-driven wind theory (Castor et al. 1975; Pauldrach et al. 1986; Friend & Abbott 1986) predicts mass-loss rates and terminal velocities as a function of stellar parameters (Abbott 1982; Vink 2000; Vink et al. 2001), and also predicts a wind momentum–luminosity relationship (WLR) (Kudritzki et al. 1995). This theory has long described the global properties of stellar winds of OBA stars. However, advances in the observational techniques (high spatial and spectral resolution) together with progress in more realistic atmosphere models have revealed discrepancies in the mass-loss rates not only between theory and observations, but also amongst different observational tracers themselves (cf. Puls et al. 2008).

^{*} Based on observations taken with the J. Sahade Telescope at Complejo Astronómico El Leoncito (CASLEO), operated under an agreement between the Consejo Nacional de Investigaciones Científicas y Técnicas de la República Argentina, the Secretaría de Ciencia y Tecnología de la Nación, and the National Universities of La Plata, Córdoba, and San Juan.

As Owocki & Rybicki (1984); Owocki et al. (1988), and later Feldmeier (1998) demonstrated, strong hydrodynamic instabilities occur in line-driven winds of massive O-type stars, leading to the formation of wind-clumping (small-scale density inhomogeneities distributed across the wind). Wind-clumping has traditionally been used to solve the issue of the mass-loss discrepancy found in O supergiants (OSGs) when different diagnostic methods are employed (Bouret et al. 2005; Fullerton et al. 2006). Mass-loss rates derived from unsaturated UV resonance lines give lower values than those obtained from the $H\alpha$ line (cf. Puls et al. 2008). The macroclumping approach (with optically thick clumps at certain frequencies) has provided a fully self-consistent and simultaneous fit to both UV and optical lines (Oskinova et al. 2007; Sundqvist et al. 2010, 2011; Šurlan et al. 2013). In previous works an artificial reduction of the stellar mass-loss rate, an extremely high clumping factor, or an anomalous chemical abundance for specific elements were invoked; however, the macroclumping approach means that none of these is necessary.

The situation is different for B supergiants (BSGs). Stellar winds of BSGs are fairly well represented by the analytical velocity β -law, with β typically in the range 1 – 3 (Crowther et al. 2006; Markova & Puls 2008). Moreover, these stars show a drop in the ratio V_∞/V_{esc} of a factor of two at around 21 000 K, from 2.6 for stars on the hot side to 1.3 for stars on the cool side (Pauldrach & Puls 1990), known as the bi-stability jump (Lamers et al. 1995). This jump was interpreted as a consequence of the recombination of Fe IV to Fe III in the wind (Vink et al. 1999). These authors predicted that this drop should be accompanied by a steep increase in the mass-loss rate of about a factor of 3 to 5, whilst some observations indicate a decrease (Crowther et al. 2006; Markova & Puls 2008). A recent study of the effects of micro- and macroclumping in the opacity behaviour of the $H\alpha$ line at the bi-stability jump suggests that the macroclumping should also play an important role at temperatures on the cool side of the jump (Petrov et al. 2014).

It is also well known that stellar winds of BSGs are highly variable. To date, most of the studies related to α Cyg variables and hypergiants have focused on their photometric and/or optical spectroscopic (mainly $H\alpha$) variability, and many surveys have been carried out to search for variability periods (e.g. Kaufer et al. 2006; Lefever et al. 2007; Lefèvre et al. 2009). Long-term space-based photometry and spectroscopy have linked this variability to opacity-driven radial and non-radial oscillations (Glatzel et al. 1999; Lefever et al. 2007; Kraus et al. 2015), and new instability domains have been established in the Hertzsprung–Russell (HR) diagram covering the region of BSGs (Saio et al. 2006; Godart et al. 2017). As massive stars can cross the BSGs’ domain more than once, the pulsation activity of these stars can drastically change between their red- and blue-ward evolution (Saio et al. 2013). BSGs on a blue-ward evolution (i.e. a post-red supergiant) tend to undergo a significantly larger number of pulsations, even including radial strange-mode pulsations with periods between 10 and 100 days (or more). It has been suggested that strange-mode pulsations cause time-variable mass-loss rates in very luminous evolved massive stars (Glatzel et al. 1999). The first observational evidence of the presence of strange modes have been found in two BSGs: HD 50064 (Aerts et al. 2010) and 55 Cyg (Kraus et al. 2015). In the latter, the authors found line variations with periods in the range of 2.7 hrs to 22.5 days. They interpreted these variations in terms of oscillations in p-, g-, and strange modes. The last could lead to phases of enhanced mass loss. Finally, the connection between pulsation and mass loss in 55 Cyg was confirmed by Yadav &

Glatzel (2016), based on a linear non-adiabatic stability analysis with respect to radial perturbations. These authors demonstrated that, as a consequence of the instabilities, the non-linear simulations revealed finite amplitude pulsations consistent with the observations.

To obtain further insights on the wind structure and wind variability of evolved stars of intermediate mass, we studied a sample of Galactic BSGs (classified either as irregular or α Cyg-type variables) in both the blue and the $H\alpha$ spectral region. The $H\alpha$ emission is quite sensitive to the wind properties (Puls et al. 2008), and we used the Fast Analysis of STellar atmospheres with WINDs (FASTWIND, Santolaya-Rey et al. 1997; Puls et al. 2005; Rivero González et al. 2012) to obtain terminal velocities and mass-loss rates by fitting synthetic to observed line profiles. In addition, to derive proper stellar parameters (effective temperature and surface gravity) we consistently modelled the Si ionization balance together with the photospheric lines of H and He. Determining new, more accurate values of mass-loss rates and stellar parameters of massive stars is crucial for our understanding of stellar wind properties, wind interactions with its surroundings, and the plausible mechanisms related with wind variability and its evolution.

The paper is structured as follows: our observations and modelling are described in Sects. 2 and 3, respectively. The results of our line profile fittings are shown in Sect. 4 and the new wind parameters are compared with previous determinations. For three objects (HD 74371, HD 99953 and HD 111973) the wind parameters are reported for the first time. As most of the stars in our sample exhibit photometric and spectroscopic variability, on timescales from one to tens of days, and have been modelled previously by several authors, in Sect. 5 we discuss changes in the wind parameters. We present for mid and late BSGs an empirical relationship between the amplitude of mass-loss variations and light/spectroscopic periods, indicating that a significant percentage of the mass-loss could be triggered by pulsation modes. Our conclusions are given in Sect. 6. Finally, Appendix A shows model fittings to the photospheric lines of each star and summarizes the stellar and wind parameters found in the literature and in this work.

2. Observations

We took high-quality optical spectra for 19 Galactic BSGs of spectral types between B0 and B9. These stars were selected from the *Bright Star Catalog* (Hoffleit & Jaschek 1991). The observations were performed in January 2006, February 2013, April 2014, and February and March 2015. We used the REOSC spectrograph (in crossed dispersion mode) attached to the *Jorge Sahade* 2.15 m telescope at the Complejo Astronómico El Leoncito (CASLEO), San Juan, Argentina. The adopted instrumental configuration was a 400 l/mm grating (#580), a single slit of width 250 μ , and a 1024x1024 TEK CCD detector with a gain of 1.98 e⁻/adu. This configuration produces spectral resolutions of $R \sim 12\,600$ at 4500 Å and $R \sim 13\,900$ at 6500 Å. Spectra were reduced and wavelength calibrated following the standard procedures using the corresponding IRAF¹ routines. The resulting spectra have an average signal-to-noise ratio (S/N) of ~ 300 .

Table 1 lists the stars in our programme, indicating name and HD number, spectral type, and variable type designation accord-

¹ IRAF is distributed by the National Optical Astronomy Observatory, which is operated by the Association of Universities for Research in Astronomy (AURA) under cooperative agreement with the National Science Foundation.

ing to Lefèvre et al. (2009) (from a study of HIPPARCOS light curves) or the VSX database. In addition, binary stars are also listed. In the following columns of the same table, we list the reported light curve or spectroscopic periods, the observation dates of our data, and the achieved wavelength coverage. Here, we present six stars with more than one observation (HD 53138, HD 58350, HD 75149, HD 80077, HD 99953, and HD 111973). One of these stars (HD 111973) was observed on two consecutive nights.

3. Stellar and wind parameters

To derive stellar and wind parameters we made use of the code FASTWIND (v10.1.7). The code computes a spherically expanding line-blanketed atmosphere. All background elements are considered with their solar abundances (taken from Grevesse & Sauval 1998). H, He, and Si atoms are treated explicitly with high precision by means of a complete NLTE approach and an accelerated lambda iteration (ALI) scheme is applied to solve the comoving-frame equations of radiative transfer (Puls 1991). The atmospheric stratification is modelled considering a smooth transition between a quasi-hydrostatic photosphere and an analytical wind structure described by a velocity β -law. The temperature structure is calculated from the electron thermal balance and is consistent with the radiative equilibrium condition.

We opted for a wind model without clumping because we want to compare the derived mass-loss rates with previous determinations and to study the wind variability. In general, mass-loss rates found in the literature are mainly estimated using unclumped models. A second reason is that we do not have contemporaneous data in the UV and IR spectral regions to evaluate the importance of the clumping factor in the $H\alpha$ line modelling. As a consequence, our results will provide upper-limit values for the mass-loss rates. In addition, to obtain an optimal fit to the observed line profiles, it was necessary to consider not only a microturbulence velocity, V_{micro} , and broadening due to the star's rotation, $V \sin i$, but also the effect of a macroturbulence velocity, V_{macro} . The latter contributes mainly to line broadening and shaping as noted by Simón-Díaz & Herrero (2007).

To obtain the effective temperature (T_{eff}) we evaluated the ionization balance (e.g. Si II–Si III, Si III–Si IV, if the Si IV $\lambda 4089, 4116$ lines are observed, and He I–He II). We used solar abundances for He and Si ($\log N_{\text{He}}/N_{\text{H}} = -1.07$ and $\log N_{\text{Si}}/N_{\text{H}} = -4.45$) and found good fits for each modelled spectrum (see details in sections §4.1 and §5). To derive an accurate determination of the surface gravity ($\log g$), we modelled the H γ and H δ lines. We used a ‘by eye’ fitting procedure to find the best-fitting synthetic line spectrum to the observed one.

The $H\alpha$ line was modelled to derive the mass-loss rate (\dot{M}) and the parameters of the velocity β -law: the power index β and the terminal velocity V_{∞} . It is important to stress that the major source of uncertainty in the determination of mass-loss rates is due to ambiguous determinations of stellar radii and distances to the stars (see Markova et al. 2004). On the other hand, $H\alpha$ is rather sensitive to V_{∞} (García et al. 2017). Therefore, the stellar radius and terminal velocities should be derived independently, as explained below.

Prior to the modelling process, the stellar radius, R_{\star} , was derived using the measured angular diameter, the distance to the star, or a fit to the observed spectral energy distribution (SED).

We model the SED with the interactive user interface BeSOS² using the best-fitting atmospheric (TLUSTY or Kurucz) model (Hubeny & Lanz 1995; Kurucz 1979). BeSOS reads stellar photometry data of any star from photometry-enabled catalogues in VizieR and the parallax distance from the HIPPARCOS catalogue. Sometimes, it was not possible to obtain a good fit to the SED (see details below on the procedures applied to each star). In these cases, a slightly modified distance was required to improve the fit. To find the best model, BeSOS uses the IDL program *mpfit* that searches for the best fit using the Levenberg–Marquardt (LM) method, which is a standard technique for solving non-linear least squares problems.

BeSOS provides, for a given colour excess, a new set of stellar parameters: T_{eff} , $\log g$, and R_{\star} (in units of the solar radius). As initial entries we use the T_{eff} and $\log g$ values obtained in this work from the Si and He ionization balances and from H γ and H δ line widths, respectively, and the code searches then for the most optimal values to fit the SED. The colour excess, $E(B - V)$, was calculated using the observed $B - V$ and the interpolated $(B - V)_0$ values calculated from the $T_{\text{eff}} - (B - V)$ scale for supergiants (Flower 1996). In a few cases, the $E(B - V)$ had to be modified to fit the 2200 Å bump properly. The stellar radius obtained using the SED is averaged with the values derived via the angular diameter and M_{bol} (the bolometric magnitude). Table 2 lists the intrinsic properties for each star: the spectral type found in the literature, the visual apparent magnitude, the observed and intrinsic colour indexes, the calculated colour excess, the stellar parameters (T_{eff} and $\log g$, obtained from fittings to the SED), the distance to the star (d), the bolometric correction (BC), the calculated bolometric magnitude, and the stellar radius. The computed parameters are listed with their corresponding errors. Details on the best-fitting model obtained with BeSOS are given in section §4.

Typical error bars derived using the BESOS code for T_{eff} , $\log g$, and R_{\star} are of about 1%, 2%, and 5%, respectively. Nevertheless, considering uncertainties in the distance estimates between 5% and 30% (from parallax measurements) and differences less than 1500 K between the T_{eff} values derived from BESOS and FASTWIND, the propagation of errors yields an uncertainty in M_{bol} lower than 10% and a margin of error between 5% and 20% for R_{\star} .

In relation to the stellar parameters derived from FASTWIND, we can adopt the parameter errors estimated by Kraus et al. (2015), who found uncertainties in T_{eff} of 300 K – 500 K from the Si ionization balance and 1000 K for the He lines. We adopt $\Delta T_{\text{eff}} = 1000$ K for those stars for which only the He lines were modelled and $\Delta T_{\text{eff}} = 500$ K if the Si II, Si III, and He lines were used to derive the temperature. From measurements of the wings of H γ and H δ we estimated an error of 0.1 dex in $\log g$. The error bars in V_{micro} are 2 km s^{−1} for Si and He lines, 5 km s^{−1} for the H lines, and 10 km s^{−1} for $H\alpha$. We model all the photospheric lines using the same V_{micro} .

Both $V \sin i$ and V_{macro} affect the line broadening. To model the line profiles we adopted the value of $V \sin i$ (± 10 km s^{−1}) found in the literature (Kudritzki et al. 1999; Lefèvre et al. 2007; Fraser et al. 2010, given in Table A.1) or average values when large scatters are present. We derived the macroturbulent velocity that reproduces the extra broadening seen in the line profile. We found uncertainties in V_{macro} from 10 km s^{−1} to 20 km s^{−1}.

² The Be Stars Observation Survey (BeSOS; <http://besos.ifa.uv.cl>) is a database containing reduced spectra acquired using the echelle spectrograph PUCHEROS.

Table 1. Log of Observations

Star Name	HD Number	Sp. Type ^a	Var. Type ^b	Period days	Observation Date (YY/MM/DD)	Wavelength Interval [Å:Å]
β Ori	34 085	B8Iae	ACYG	2.075 ^c , 1.22-74.74 ^d , 28 ⁿ	2006/01/15	[3500:7850]
κ Ori	38 771	B0.5Ia	IA	1.047 ^e , 1.9 ^f , 4.76 ^e , 6.5 ^f , 9.5 ^f	2006/01/15	[3500:7850]
χ^2 Ori	41 117	B2Ia	ACYG	0.92 ^e , 0.95 ^e , 2.869 ^e , 20 ^e , 40 ^e , 200 ^e	2006/01/15	[3500:7850]
PU Gem	42 087	B4Ia ^g	ACYG	6.807 ^o , 25 ^e	2006/01/15	[6500:7850]
V731 Mon	47 240	B1Ib	ACYG, SB ^q	1.73 ^j , 2.742 ^{c,e} , 133 ^e	2006/01/15	[3500:7850]
ϵ CMa	52 089	B1.5 II	IA		2013/02/05	[4300:6850]
V820 Cas	52 382	B1Ia	IA		2006/01/15	[3500:7850]
σ^2 CMa	53 138	B3Ia	ACYG	3.69 ^j , 24.39 ^j , 24.44 ^c	2006/01/15	[3500:7850]
η CMa	58 350	B5Ia	L, ACYG	4.7 ⁱ , 6.631 ^j	2013/02/05	[4300:6850]
					2006/01/15	[3500:7850]
					2013/02/05	[4300:6850]
J Pup	64 760	B0.5Ib	IA	1.2 ^m , 1.8 ^j , 2.4 ^m , 2.8 ^j , 6.8 ^m	2013/02/05	[4300:6850]
LN Vel	74 371	B6Iab/b	IA, ACYG	8.29 ^{c,i} , 1, 15-20 ^h	2006/01/15	[3500:7850]
OP Vel	75 149	B3Ia	SPB?, ACYG	1.086 ^{c,n} , 1.215 ^j , 2.214 ^j	2006/01/15	[3500:7850]
					2013/02/05	[4300:6850]
					2013/02/07	[4300:6850]
					2014/04/14	[4200:6650]
GX Vel	79 186	B5Ia	IA		2006/01/15	[3500:7850]
PV Vel	80 077	B2Ia+e	GCAS?, SDOR	3.115 ^c , 21.2 ^l , 41.5 ^h , 55.5 ^h , 66.5 ^h , 76.0 ^h	2006/01/15	[3500:7850]
					2014/04/12	[4200:6650]
					2013/02/05	[4300:6850]
V519 Car	92 964	B2.5Ia	ACYG	2.119 ^j , 4.71 ^c , 14.706 ^j	2013/02/05	[4300:6850]
V808 Cen	99 953	B1/2Iab/b	IA	17.7 ^k	2014/04/14	[4200:6650]
					2015/02/13	[4200:6650]
					2015/03/13	[4200:6650]
κ Cru	111 973	B2/3Ia	ACYG?, IA, SB ^p	9.536 ⁱ , 57.11 ⁱ	2014/04/11	[4200:6650]
					2014/04/12	[4200:6650]
					2014/04/11	[4200:6650]
ALS 3038	115 842	B0.5Ia/ab	ACYG?, IA	10.309 ^c , 13.38 ⁱ	2014/04/11	[4200:6650]
V1058 Sco	148 688	B1Iaep	ACYG	1.845 ^c , 6.329 ^c	2014/04/11	[4200:6650]

Notes. ^(a) From the SIMBAD astronomical database (Wenger et al. 2000). ^(b) IA (poorly studied variables of early spectral type), L (slow irregular variables), GCAS (γ Cassiopeiae type), ACYG (α Cyg type), SPB (slowly pulsating B stars), and S Dor (S Doradus type) (classification taken from Lefèvre et al. 2009). The question mark means that the classification was based on a new period determination or that the type could not be clearly identified from the HIPPARCOS light curve. ^(c) Lefèvre et al. (2009), ^(d) Moravveji et al. (2012), ^(e) Morel et al. (2004), ^(f) Prinja et al. (2004), ^(g) this work, ^(h) van Genderen et al. (1989), ⁽ⁱ⁾ Koen & Eyer (2002), ^(j) Lefèvre et al. (2007), ^(k) Sterken (1977), ^(l) Knoechel & Moffat (1982), ^(m) Kaufer et al. (2006), ⁽ⁿ⁾ Aerts et al. (2013), ^(o) International Variable Star Index (VSX) database, and ^(p,q) SB (spectroscopic binary Chini et al. 2012; Prinja et al. 2002).

Regarding the wind parameters, we searched for V_∞ measurements from UV observations (Prinja & Massa 2010; Prinja et al. 1998; Howarth et al. 1997) and used them as initial values to reproduce the $H\alpha$ line. Good fits were obtained using slight variations of V_∞ . These values are listed in Table 3 with deviations of 10% with respect to the UV measurements. In a few cases, the UV terminal velocities were not able to fit the observed $H\alpha$ line profile and our own V_∞ determinations are provided. In this case, the discrepancies obtained between the derived V_∞ and the UV data can increase up to 30%. Therefore, we consider errors for V_∞ between 10% and 30%.

Adopting the values for V_∞ from the UV and errors of 10% for R_\star , we observe that late and early B supergiants may show a change of up to 20% in the equivalent width (EW) of the emission component of a P Cygni line profile if \dot{M} varies by an amount of 10% and 20%, respectively. Larger errors in V_∞ might give uncertainties on \dot{M} of 30%. However, when the $H\alpha$ line is seen in absorption, the error on \dot{M} can be larger than a factor of 2 (Markova et al. 2004).

4. Results

For each star in our programme we modelled the line profiles of H, He, and Si. Figure 1 shows the observed $H\alpha$ line and the

best-fitting synthetic model. The rest of the lines and their corresponding fits are shown in the Appendix (Figs. A.1-A.7). In Table 3 we list the obtained stellar and wind parameters with their errors: T_{eff} , $\log g$, β , \dot{M} , V_∞ , V_{micro} , V_{macro} , $V \sin i$, R_\star (stellar radius in solar radius units), $\log L/L_\odot$ (stellar luminosity referenced to the solar value), $\log D_{\text{mom}}$ (the modified wind momentum rate, see section §5), $\log L/M$ (both L and M in solar units, where M is the stellar mass), and Q (optical-depth invariant, discussed in section §5). The parameters V_{micro} and V_{macro} are related to the photospheric lines. Initially V_{micro} was fixed at 10 km s⁻¹ and then varied by ± 5 km s⁻¹ to achieve the best fit to the intensities of He and Si lines.

The photospheric lines of each star (at a given epoch) were modelled with the same set of V_{micro} and V_{macro} values. However, to properly match the $H\alpha$ and He I λ 6678 line widths and shapes we often needed a different turbulent velocity since these lines are affected by the velocity dispersion of the flow.

Regarding the determination of the wind parameters, we were able to reproduce the $H\alpha$ line of many BSGs. However, in a few cases, even when the emission component of the PCygni profile looked well fitted, it was impossible to reproduce the intensity of the absorption component. Similar problems were found when reproducing the $H\alpha$ absorption profile of HD 38771, HD 75149, and HD 111973 because of the presence of an incip-

Table 2. Stellar parameters calculated in the present study or adopted from the literature

HD Number	ST	m_V	$B - V$	$(B - V)_0^a$	$E(B - V)$	T_{eff} K	$\log g$ dex	d pc	BC^a	M_{bol}	R_\star R_\odot
34 085	B8 Iae	0.13	-0.03	-0.07	0.04	$11\,760 \pm 120$	2.00 ± 0.10	264 ± 23	-0.83	-7.9 ± 0.2	72 ± 10
38 771	B0.5 Ia	2.06	-0.18	-0.23	0.05	$25\,700 \pm 260$	2.70 ± 0.05	198 ± 8	-2.41	-7.0 ± 0.2	13 ± 1
41 117	B2 Ia	4.63	0.28	-0.18	0.42	$17\,940 \pm 180$	2.20 ± 0.05	552 ± 85	-1.84	-7.3 ± 0.4	23 ± 3
42 087	B4 Ia	5.78	0.20	-0.14	0.34	$15\,000 \pm 150$	2.39 ± 0.05	$2\,075 \pm 1\,000^s$	-1.46	-8.3 ± 1.1	55 ± 11
47 240	B1 Ib	6.15	0.15	-0.18	0.33	$17\,500 \pm 180$	2.40 ± 0.05	$1\,598 \pm 479$	-1.78	-7.7 ± 0.7	30 ± 4
52 089	B1.5 II	1.50	-0.21	-0.20	0.00	$21\,000 \pm 210$	3.00 ± 0.05	124 ± 2	-2.20	-6.2 ± 0.1	11 ± 1
52 382	B1 Ia	6.50	0.19	-0.20	0.44	$23\,140 \pm 230$	2.47 ± 0.05	$1\,301 \pm 430^s$	-2.05	-7.5 ± 0.8	21 ± 2
53 138	B3 Ia	3.02	-0.08	-0.21	0.10	$18\,000 \pm 180$	2.20 ± 0.05	847 ± 287	-1.66	-8.5 ± 0.8	46 ± 4
58 350	B5 Ia	2.45	-0.09	-0.17	0.08	$15\,000 \pm 500^f$	2.00 ± 0.10^f	609 ± 148	-1.24	-8.0 ± 0.6	54 ± 6
64 760	B0.5 Ib	4.24	-0.14	-0.21	0.07	$22\,370 \pm 220$	2.50 ± 0.05	507 ± 25	-2.21	-6.7 ± 0.2	12 ± 1
74 371	B6 Iab/b	5.23	0.20	-0.15	0.35	$13\,800 \pm 140$	2.00 ± 0.05	$1\,800 \pm 360^s$	-1.02	-8.7 ± 0.5	73 ± 10
75 149	B3 Ia	5.46	0.27	-0.19	0.46	$15\,000 \pm 150$	2.12 ± 0.05	$1\,642 \pm 330^s$	-1.39	-8.4 ± 0.7	61 ± 13
79 186	B5 Ia	5.00	0.22	-0.13	0.35	$15\,000 \pm 150$	2.12 ± 0.05	$1\,449 \pm 609$	-1.36	-8.3 ± 0.9	61 ± 7
80 077	B2Ia+e	7.56	1.34	-0.16	1.50	$18\,000 \pm 180$	2.17 ± 0.05	$3\,600 \pm 600^s$	-1.62	-11.6 ± 0.4	195 ± 47
92 964	B2.5Ia	5.38	0.27	-0.16	0.48	$18\,000 \pm 180$	2.19 ± 0.05	$1\,851 \pm 994$	-1.66	-9.1 ± 1.2	70 ± 14
99 953	B1/2 Iab/b	6.5	0.38	-0.18	0.56	$18\,830 \pm 190$	2.30 ± 0.05	$1\,075 \pm 427$	-1.78	-7.2 ± 0.9	25 ± 3
111 973	B2/3 Ia	5.94	0.24	-0.14	0.38	$17\,180 \pm 170$	2.18 ± 0.05	$1\,660 \pm 350^s$	-1.46	-7.8 ± 0.5	46 ± 9
115 842	B0.5 Ia/ab	6.03	0.30	-0.23	0.60	$25\,830 \pm 260$	2.75 ± 0.05	$1\,538 \pm 750$	-2.46	-9.2 ± 1.2	35 ± 4
148 688	B1 Iaeqp	5.31	0.35	-0.20	0.54	$20\,650 \pm 210$	2.20 ± 0.05	833 ± 229	-2.00	-8.0 ± 0.7	31 ± 4

Notes.

Values of T_{eff} and $\log g$ were derived by fitting the SED, with the exception of those flagged with f .

R_\star is an average of the values obtained from three different approaches (see details in section §3).

d is the distance to the star in parsecs derived from HIPPARCOS, with the exception of those data flagged with s .

(a)

BC: bolometric correction taken from Flower (1996),

(f)

parameters derived with the code FASTWIND (see details in section §4.1), and

(s)

distances derived from other methods, see details in the text.

ient emission in the line core. Contrary to the $H\alpha$ line, synthetic line profiles of the photospheric lines match the observations very well.

4.1. Comments on individual objects

In the following we summarize the previous and current data of the stellar and wind parameters for each star. In addition, we complement our data with images taken with the Wide-field Infrared Survey Explorer (WISE) (Wright et al. 2010), covering the range $3.5 \mu - 22 \mu$ (bands W1 and W4). These images are used to identify former phases of strong stellar winds.

HD 34085 is a B8 Iae star that has been studied by many authors. Using FASTWIND we estimated the stellar fundamental parameters: $T_{\text{eff}} = 12\,700$ K and $\log g = 1.7$. The best-fitting model to the SED was obtained with the BeSOS interactive interface using a Kurucz model with $T_{\text{eff}} = 11\,760$ K, $\log g = 2.0$, $R_\star = 71 R_\odot$, $E(B - V) = 0.044$ (calculated as explained in section §3), and $d = 259$ pc (which is close to the distance of 264 pc given by HIPPARCOS). Using the HIPPARCOS distance and the mentioned value of $E(B - V)$, we estimated $M_{\text{bol}} = -7.95$ mag and $R_\star = 70 R_\odot$; instead, from the angular diameter (2.713 mas, Zorec et al. 2009) we calculated $R_\star = 76 R_\odot$. We assumed a mean value for this star of $R_\star = 72 R_\odot$.

Our estimate of T_{eff} (12 700 K) agrees with previous determinations (see Table A.1). This star shows a photometric variation of 2.075 days (Lefèvre et al. 2009). Moreover, Moravveji et al. (2012) found 19 significant pulsation modes from radial velocities with variability timescales ranging from 1.22 days to

74.74 days. It also presents a variable stellar wind with changes in the mass-loss rate of at least 20% on a timescale of one year (Chesneau et al. 2014). Using spectro-interferometric monitoring, these authors found time variations in the differential visibilities and phases. For some epochs, the temporal evolution of the signal suggests the rotation of circumstellar structures. However, at some periods, no phase signal was observed at all. This result was interpreted in the context of second-order perturbations of an underlying spherical wind.

The $H\alpha$ line is highly variable (with profiles in absorption, filled in by emission, double-peaked, or inversed P Cygni; Chesneau et al. 2014). Our observation resembles the one reported by Przybilla et al. (2006). Our estimate for the mass-loss rate is ~ 1.5 times lower than the value obtained by Markova et al. (2008), and at least one-third of the value reported by Chesneau et al. (2014). We also derive a low terminal velocity. This value is quite uncertain because we were not able to fit the absorption component of the $H\alpha$ P Cygni profile. Moreover, a high V_{macro} (85 km s^{-1}) was needed to reproduce the emission component of the line profile. The photospheric lines were modelled very well, with the exception of the $\text{He I } \lambda 4471$ line, which does not exhibit the forbidden component.

HD 38771 (B0.5Ia): The stellar and wind parameters of this star have been derived by many authors: Nerney (1980); Garmann et al. (1981); Lamers et al. (1982); Kudritzki et al. (1999); Crowther et al. (2006); Searle et al. (2008); Zorec et al. (2009). Their values range from 26 000 K to 27 500 K in T_{eff} , from 2.9 dex to 3.07 dex in $\log g$, from $13.0 R_\odot$ to $28 R_\odot$ in stellar radius, from $0.27 \times 10^{-6} M_\odot \text{ yr}^{-1}$ to $1.20 \times 10^{-6} M_\odot \text{ yr}^{-1}$ in \dot{M} ,

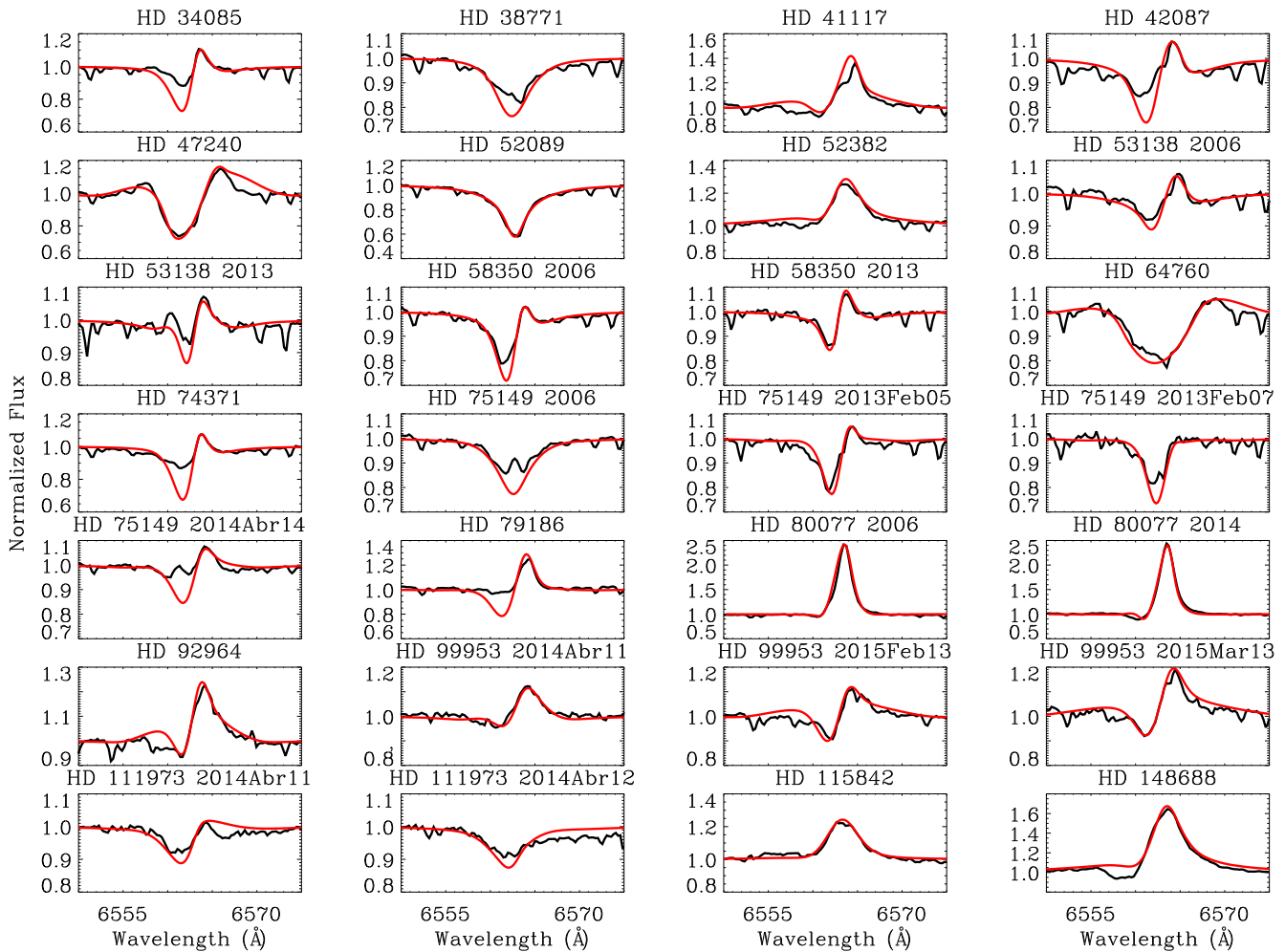


Fig. 1. $H\alpha$ line and the best-fitting synthetic model. For HD 53138, HD 58350, HD 75149, HD 80077, HD 99953, and HD 111973 more than one plot are shown due to multi-epoch observations.

and from $1\,350\,\text{km s}^{-1}$ to $1\,870\,\text{km s}^{-1}$ in V_∞ (see Table A.1). The star presents a variable magnetic field (Nerney 1980) and exhibits spectral variations. The observed $H\alpha$ line is quite variable, showing a pure absorption profile (Kudritzki et al. 1999), a double-peaked absorption profile with a central emission (Rusconi et al. 1980), and an absorption profile with a strong central emission (Crowther et al. 2006). Morel et al. (2004) also described changes in morphology and profile amplitude of 32.6%, which clearly suggest variations in the wind conditions. These authors also found two photometric periods of 4.76 days and 1.047 days and Prinja et al. (2004) reported additional spectroscopic periods of 1.9 days, 6.5 days, and 9.5 days.

At the time of our observation the $H\alpha$ line displayed an asymmetric absorption profile with a weak emission in the core (Fig. 1). We also note that the core of the $H\beta$ line might be filled in by an incipient emission (Fig. A.1). Extra broadening effects are present in all the photospheric lines leading to large V_{macro} estimates (of the order of the projected rotation velocity).

We derived $T_{\text{eff}} = 25\,000\,\text{K}$ using Si II and Si III , and also using the He I and He II ionization balance. The best-fitting SED model was obtained with a TLUSTY model for $T_{\text{eff}} = 25\,700\,\text{K}$, $\log g = 2.70$, $R_\star = 14\,R_\odot$, and $E(B - V) = 0.05\,\text{mag}$ for a distance of 191 pc (close to the HIPPARCOS distance of $d_H = 198\,\text{pc}$; van Leeuwen 2007). Using d_H in Pogson's formula we derived a $M_{\text{bol}} = -6.99\,\text{mag}$ and $R_\star \sim 12\,R_\odot$. The adopted stellar radius, $R_\star \sim 13\,R_\odot$, which is consistent with the value derived

from the angular diameter calculated by Zorec et al. (2009, 0.62 mas).

Our T_{eff} value is 1 000 K lower than the values obtained by Searle et al. (2008) and Gathier et al. (1981), while the stellar radius is similar to that obtained by Kudritzki et al. (1999). Compared with previous determinations, our mass-loss rate has the lowest value. As $H\alpha$ is in pure absorption \dot{M} might have a large uncertainty.

Considering the diversity of the stellar and wind parameters found in the literature, and that the $H\alpha$ line profile shows important variations, this star is a good candidate to search for pulsating or magnetic activity connected to cyclic wind variability.

HD 41117 (B2Ia): This is another deeply studied star (Zorec et al. 2009; Crowther et al. 2006; Morel et al. 2004; Kudritzki et al. 1999; Scuderi et al. 1998; Nerney 1980). Morel et al. (2004) found $H\alpha$ variations, both in shape and intensity, and reported light variability on a period of 2.869 days. Additional sets of spectroscopic periods were obtained from $H\alpha$ equivalent width time series (Morel et al. 2004, Table 1).

From Table A.1 we see that the fundamental stellar parameters and luminosity are consistent with those already published, in contrast with the wind parameters (mainly \dot{M}) that are quite different (by a factor of up to 3.6).

The best-fitting SED model corresponds to $T_{\text{eff}} = 17\,940\,\text{K}$, $\log g = 2.2$, $R_\star = 26\,R_\odot$, $E(B - V) = 0.42\,\text{mag}$ (instead we

Table 3. Stellar and wind parameters derived from line fitting procedures.

STAR	T_{eff} K	$\log g$ dex	β	\dot{M} $10^{-6} M_{\odot} \text{ yr}^{-1}$	V_{∞} km s^{-1}	V_{macro} km s^{-1}	V_{micro} km s^{-1}	$V \sin i$ km s^{-1}	R_{\star} R_{\odot}	$\log(L/L_{\odot})$ dex	$\log D_{\text{mom}}$ dex	$\log(L/M)$ dex	$\log Q$ dex
HD 34085	12 700 ± 500	1.70 ± 0.1	2.6	0.23±0.02	155±46	52±3	10 ± 2	30	72	5.09 ± 0.09	27.22 ± 0.19	4.13	-12.71 ± 0.32
HD 38771	25 000 ± 1 000	2.70 ± 0.1	1.5	0.14±0.04	1500±150	60±10	13 ± 2	80	13	4.78 ± 0.07	27.69 ± 0.19	4.27	-13.29 ± 0.24
HD 41117	19 000 ± 1 000	2.30 ± 0.1	2.0	0.17±0.03	510±51	65±20	10 ± 5	40	23	4.84 ± 0.16	27.38 ± 0.15	4.27	-12.78 ± 0.23
HD 42087	16 500 ± 1000	2.45 ± 0.1	2.0	0.57±0.05	700±70	80±15	15 ± 5	80	55	5.31 ± 0.43	28.27 ± 0.13	3.83	-13.12 ± 0.23
HD 47240	19 000 ± 1000	2.40 ± 0.1	1.0	0.24±0.02	450±90	60±10	10 ± 3	95	30	5.03 ± 0.30	27.57 ± 0.15	4.08	-12.82 ± 0.26
HD 52089	23 000 ± 1 000	3.00 ± 0.1	1.0	0.02±0.006	900±270	65±5	8 ± 2	10	11	4.49 ± 0.05	26.58 ± 0.28	3.88	-13.69 ± 0.38
HD 52382	21 500 ± 1 000	2.45 ± 0.1	2.2	0.24±0.04	1 000±100	65±5	10 ± 2	55	21	4.94 ± 0.32	27.84 ± 0.14	4.29	-13.10 ± 0.21
HD 53138	18 000 ± 1000	2.25 ± 0.2	2.0	0.24±0.02	600±120	50±10	10 ± 4	40	46	5.31 ± 0.32	27.79 ± 0.14	4.19	-13.09 ± 0.22
	18 000 ± 1000	2.25 ± 0.2	2.0	0.20±0.01	450±135	60±5	9 ± 3	40	46	5.31 ± 0.32	27.59 ± 0.14	4.19	-13.36 ± 0.22
HD 58350	15 000 ± 500	2.00 ± 0.1	3.0	0.15±0.02	233 ± 23	70±10	12 ± 2	40	54	5.13 ± 0.23	27.21 ± 0.13	4.12	-12.97 ± 0.20
	16 000 ± 500	2.00 ± 0.1	3.0	0.12±0.01	175±18	50±10	10 ± 5	40	54	5.24 ± 0.23	26.98 ± 0.13	4.23	-12.90 ± 0.20
HD 64760	23 000 ± 1 000	2.90 ± 0.1	0.5	0.42±0.06	1 500 ± 150	100 ± 50	15 ± 5	230	12	4.57 ± 0.08	28.14 ± 0.12	3.73	-12.76 ± 0.18
HD 74371	13 700 ± 500	1.80 ± 0.1	2.0	0.28±0.03	200±60	60±10	10 ± 3	30	73	5.23 ± 0.19	27.48 ± 0.21	4.17	-12.80 ± 0.33
HD 75149	16 000 ± 1 000	2.10 ± 0.1	2.5	0.09±0.03	400±40	62±12	9 ± 3	40	61	5.35 ± 0.29	27.25 ± 0.11	4.14	-13.63 ± 0.22
	16 000 ± 1 000	2.10 ± 0.1	2.5	0.20±0.01	350±35	52±12	11 ± 1	40	61	5.35 ± 0.29	27.54 ± 0.11	4.14	-13.19 ± 0.22
	16 000 ± 1 000	2.10 ± 0.1	2.5	0.16±0.05	400±40	57±7	17 ± 1	40	61	5.35 ± 0.29	27.50 ± 0.11	4.14	-13.37 ± 0.22
	16 000 ± 1 000	2.10 ± 0.1	2.5	0.25±0.01	350±35	55±10	15 ± 1	40	61	5.35 ± 0.29	27.64 ± 0.11	4.14	-13.10 ± 0.22
HD 79186	15 800 ± 500	2.00 ± 0.1	3.3	0.40±0.02	400±40	53±7	11 ± 1	40	61	5.33 ± 0.38	27.90 ± 0.11	4.21	-12.98 ± 0.20
HD 80077	17 700 ± 1 000	2.20 ± 0.1	3.2	5.4±0.50	200±20	10	195	6.53 ± 0.17	28.86 ± 0.14	4.23	-12.15 ± 0.26
	17 700 ± 1 000	2.20 ± 0.1	3.0	5.4±0.50	150±15	60±5	10 ± 5	10	195	6.53 ± 0.17	28.98 ± 0.14	4.23	-11.97 ± 0.26
HD 92964	18 000 ± 1 000	2.20 ± 0.1	2.0	0.49±0.03	370±55	40±5	11 ± 1	45	70	5.67 ± 0.49	27.98 ± 0.13	4.25	-12.93 ± 0.25
HD 99953	19 000 ± 1 000	2.30 ± 0.1	2.0	0.08±0.01	250±50	50±5	18 ± 2	50	25	4.87 ± 0.37	26.80 ± 0.14	4.22	-12.79 ± 0.24
	19 000 ± 1 000	2.30 ± 0.1	2.0	0.13 ± 0.01	500±100	50 ± 5	18 ± 2	50	25	4.87 ± 0.37	27.33 ± 0.14	4.22	-13.03 ± 0.24
	19 000 ± 1 000	2.30 ± 0.1	2.0	0.22 ± 0.01	700±140	50 ± 5	18 ± 2	50	25	4.87 ± 0.37	27.69 ± 0.14	4.22	-13.02 ± 0.24
HD 111973	16 500 ± 1 000	2.10 ± 0.1	2.0	0.21 ± 0.01	350±70	57±8	12 ± 2	35	46	5.16 ± 0.20	27.51 ± 0.15	4.19	-13.02 ± 0.27
	16 500 ± 1 000	2.10 ± 0.1	2.0	0.14 ± 0.004	350 ± 105	63±3	12 ± 2	35	46	5.16 ± 0.20	27.33 ± 0.15	4.19	-13.19 ± 0.27
HD 115842	25 500 ± 1 000	2.75 ± 0.1	2.5	1.80±0.30	1 700±340	63±3	23 ± 7	50	35	5.67 ± 0.62	29.06 ± 0.18	4.30	-12.91 ± 0.28
HD 148688	21 000 ± 1 000	2.45 ± 0.1	2.5	1.15±0.20	1 200±360	65±5	11 ± 1	50	31	5.23 ± 0.28	28.69 ± 0.23	4.26	-12.80 ± 0.36

derived $E(B - V) = 0.46$ mag from Flower 1996) and $d = 477$ pc (while the distance measured by HIPPARCOS is 552 ± 85 pc). On the other hand, using $d = 447$ pc and $E(B - V)$, the angular diameter (0.371 mas, Zorec et al. 2009), or the computed bolometric magnitude (-7.35 mag) the stellar radius is $R_{\star} \sim 23 R_{\odot}$. We therefore adopted $R_{\star} = 23 R_{\odot}$, which is also consistent with the stellar radius expected from the HIPPARCOS distance. The stellar radius is lower than the value derived by other authors (see Table A.1); however, if we use the distance derived by Megier et al. (2009, 1.62 kpc) we obtain $R_{\star} = 62 R_{\odot}$.

From the line modelling we obtained higher $T_{\text{eff}} = 19 500$ K and $\log g = 2.3$ values. Our spectrum reveals a $H\alpha$ emission line with a complex blue-ward absorption component (see Fig. 1). The mass-loss rate derived here is lower (by a factor of about 5) than the value reported by Kudritzki et al. (1999). We also obtained a lower terminal velocity. The rest of the lines are in pure absorption and are excellently modelled (see Fig. A.1). Values of V_{micro} and V_{macro} as high as the rotational velocity of the star ($V \sin i = 40 \text{ km s}^{-1}$) are needed to reproduce the extra broadening of the photospheric lines. A larger macroturbulent velocity (65 km s^{-1}) was also obtained by Simón-Díaz & Herrero (2014).

HD 42087 (B4Ia): The SED was fitted with a TLUSTY model using $T_{\text{eff}} = 15 000$ K, $\log g = 2.39$, $R_{\star} = 60 R_{\odot}$, $E(B - V) = 0.34$ mag, and $d = 2021$ pc (which is similar to the distance of 2075 pc derived by Megier et al. 2009, from the Ca II H+K lines). On the other hand, a distance $d = 2075$ pc gives $M_{\text{bol}} = -8.33$ mag and $R_{\star} = 50 R_{\odot}$, while the angular distance calculated by Zorec et al. (2009) leads to $R_{\star} = 57 R_{\odot}$. We adopted a mean value of $R_{\star} = 55 R_{\odot}$.

Our optical spectrum only covers the $H\alpha$ region; therefore, we were not able to determine the effective temperature using the silicon lines. Thus, we adopted the value calculated by Zorec

et al. (2009) ($T_{\text{eff}} = 16 500$ K) and derived from the H lines a $\log g = 2.45$. This T_{eff} is lower than the value reported by Benaglia et al. (2007) and Searle et al. (2008), and greater than the value we derived from the fitting of the SED.

This star presents a significant $H\alpha$ variability of 91.2% and both the $H\alpha$ and $\text{He I } \lambda 6678$ lines show a cyclic behaviour on a periodicity of ~ 25 days (Morel et al. 2004). This period is larger than the 6.807-day period found from the HIPPARCOS light curve (Morel et al. 2004; Lefèvre et al. 2009).

Our $H\alpha$ line shows a P Cygni feature with a weak emission and a broad absorption component with a superimposed incipient emission structure. We fitted the $H\alpha$ line profile using a wind model with $\dot{M} = 0.57 \cdot 10^{-6} M_{\odot} \text{ yr}^{-1}$ and $V_{\infty} = 700 \text{ km s}^{-1}$. The obtained V_{∞} is similar to the one measured in the UV spectral range (735 km s^{-1} , Howarth et al. 1997).

HD 47240 is a fast rotating B1Ib star ($V \sin i = 114 \text{ km s}^{-1}$, Simón-Díaz & Herrero 2014) that lies behind the Monoceros Loop supernova remnant (SNR). It presents very broad photospheric absorption lines, periodic light variations of 2.742 days (Lefèvre et al. 2009; Morel et al. 2004), periodic motions due to binarity, and the presence of discrete absorption components (DACs, Prinja et al. 2002) that appear double. We were able to get a good fit to the SED for the following parameters: $T_{\text{eff}} = 17 500$ K, $\log g = 2.4$, $E(B - V) = 0.33$ mag, $d = 1515$ pc, and $R_{\star} = 35 R_{\odot}$. The derived distance is consistent with the distance estimate of 1598 pc by Megier et al. (2009) and the colour excess also matches the 2200 Å bump. We also calculated a $M_{\text{bol}} = -7.66$ mag and $R_{\star} = 28 R_{\odot}$ (for $d = 1598$ pc). This stellar radius agrees with the computed value from the angular diameter (0.157 mas) by Zorec et al. (2009). We adopted a mean value of $R_{\star} = 30 R_{\odot}$.

The stellar parameters derived with FASTWIND agree with the values given in one of the models calculated by Lefever et al. (2007) (who found two models with very different T_{eff} and $\log g$ and both fit very well the Si III line profiles). The T_{eff} obtained here is lower than the 21 670 K derived with the BCD spectrophotometric method (Zorec et al. 2009).

To model the photospheric lines we needed a high V_{macro} value (60 km s^{-1}) that is much higher than those used to model the H lines formed in the wind (3 km s^{-1}). As this object is a pulsating variable star of α Cyg type, a high V_{macro} value is expected.

Our spectrum shows $H\alpha$ as a double-peaked emission line with an intense central absorption. This profile was considered as an indicator of the presence of a disk-like structure (Lefever et al. 2007). We achieved a good fit to the observed $H\alpha$ line for the intensity of the absorption and for the two emission components. We derived a mass-loss rate of $2.4 \times 10^{-7} M_{\odot} \text{ yr}^{-1}$. This value agrees with the upper limit of the range reported by Lefever et al. (2007, $1.7 \times 10^{-7} M_{\odot} \text{ yr}^{-1} - 2.4 \times 10^{-7} M_{\odot} \text{ yr}^{-1}$) and is lower than the value calculated by Morel et al. (2004, $0.31 \times 10^{-7} M_{\odot} \text{ yr}^{-1}$) from the theoretical WLR for OBA supergiants. For the terminal velocity, we found almost half of the value obtained by Lefever et al. (2007); Prinja & Massa (2013).

HD 52089 (B1.5 II) is the brightest EUV source in the sky. It shows a UV emission line spectrum and X-ray emission consistent with a wind-shock model. Using the observed SED and TLUSTY models we derived $T_{\text{eff}} = 21\,000 \text{ K}$, $\log g = 3.0$, and $R_{\star} = 11 R_{\odot}$ for a distance of 124 pc (van Leeuwen 2007) and $E(B - V) = 0.00 \text{ mag}$. This stellar radius is also consistent with the bolometric magnitude ($M_{\text{bol}} = -6.18 \text{ mag}$) and the measurement of the angular diameter (0.801 mas , Zorec et al. 2009) that lead to $10 R_{\odot}$ and $10.6 R_{\odot}$, respectively. From FASTWIND we derived a higher T_{eff} ($23\,000 \text{ K}$) that agrees with the values given in Lefever et al. (2010); Zorec et al. (2009), and Morel et al. (2008), but it is higher than the value of $20\,100 \text{ K}$ obtained by Fraser et al. (2010). Our surface gravity value (3 dex) agrees more closely with the Fraser et al. (2010) estimate and it is 0.2 dex lower than those reported by Lefever et al. (2010) and Morel et al. (2008). The star has a longitudinal magnetic field of 149 G (Morel et al. 2008). Our spectrum displays all the H lines in absorption. Using optical data we derive a mass-loss rate of $2 \times 10^{-8} M_{\odot} \text{ yr}^{-1}$, which is similar to the value obtained phenomenologically by Cohen et al. (1996, $3 \times 10^{-8} M_{\odot} \text{ yr}^{-1} - 8 \times 10^{-8} M_{\odot} \text{ yr}^{-1}$).

HD 52382 (B1Ia) is an O-B2 runaway candidate (Peri et al. 2012). Using FASTWIND to fit the ratios of Si III/Si II and He II/He I we obtain $T_{\text{eff}} = 21\,500 \text{ K}$, and from the H γ and H δ lines a $\log g = 2.45$. From Flower (1996) we have $(B - V)_0 = -0.20 \text{ mag}$ and derive a colour excess of 0.39 mag . The best fit to the observed SED corresponds to a TLUSTY model with $T_{\text{eff}} = 23\,140 \text{ K}$, $\log g = 2.47$, $R_{\star} = 21.6 R_{\odot}$, and $d = 1.23 \text{ kpc}$, but with a larger $E(B - V) = 0.44 \text{ mag}$. This distance agrees with the 1.1 kpc found by Megier et al. (2009) and with the parallactic distance of 1.3 kpc measured by Gaia (0.768 mas ; Astraatmadja & Bailer-Jones 2016). Using the distance of 1.3 kpc in Pogson's formula and the expression for the angular radius (with 0.17 mas ; Pasinetti Fracassini et al. 2001), we obtain a stellar radius of $18.6 R_{\odot}$ and $23.5 R_{\odot}$, respectively. Therefore, we adopted $R_{\odot} = 21 R_{\odot}$ as the mean value. We rejected the HIPPARCOS distance of 471 pc because it leads to a value of M_{bol} that is too low for a B supergiant.

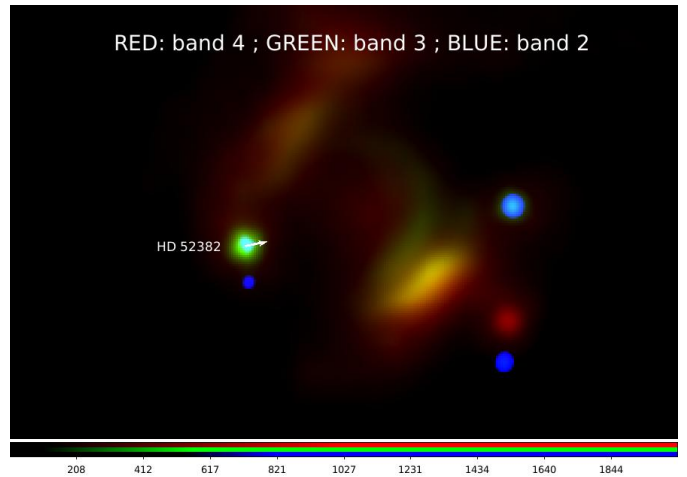


Fig. 2. WISE images (W2 = $4.6 \mu\text{m}$ in blue, W3 = $12 \mu\text{m}$ in green, and W4 = $22 \mu\text{m}$ in red) showing a bow-shock structure near HD 52382. The white arrow indicates the direction of the proper motion of the star.

The derived $T_{\text{eff}} = 21\,500 \text{ K}$ is between the values calculated by Lefever et al. (2010) and Krtićka & Kubát (2001). The star presents a variable $H\alpha$ line profile displaying a P Cygni or a pure emission feature (Morel et al. 2004). Our spectrum shows a pure emission line. We were able to reproduce all the spectral lines very well. We derived a terminal velocity of $1\,000 \text{ km s}^{-1}$, which is of the same order as that obtained from the UV region (900 km s^{-1} , Prinja et al. 1990), but 200 km s^{-1} lower than the value found by Krtićka & Kubát (2001) for a similar mass-loss rate. The combined WISE W2, W3, and W4 images (Fig. 2, at $4.6 \mu\text{m}$, $12 \mu\text{m}$, and $22 \mu\text{m}$, respectively) reveal a complex structure close to the star and in the direction of its proper motion (indicated in Fig. 2 with a white arrow) that could be related to wind interactions with the ISM, due to high mass-loss episodes in the past.

We want to stress that for an optimal fitting of the photospheric lines we have to introduce high values of V_{macro} , of around 65 km s^{-1} (a similar result was reported by Lefever et al. 2010), which could be an indication of pulsation activity. The He I $\lambda 6678$ line shows a little emission in the core.

HD 53138 (B3Ia) has been studied by several authors (see summary in Table A.1). The derived T_{eff} ranges from $15\,400 \text{ K}$ to $18\,500 \text{ K}$, and $\log g$ from 2.05 dex to 2.35 dex . The star exhibits irregular variations in the $H\alpha$ line (Morel et al. 2004). Our spectra also show variations: in 2006 the star displayed a typical P Cygni profile, while in 2013 a double-peaked emission was observed. We also note differences in the intensities and line widths of the H γ and the Si III lines for the two epochs that lead to slightly different values of T_{eff} and $\log g$. We obtained for both epochs the following fundamental parameters: $18\,000 \text{ K}$ for T_{eff} and 2.25 dex for $\log g$ with uncertainties of $1\,000 \text{ K}$ and 0.2 dex . The best-fitting SED model suggests $T_{\text{eff}} = 18\,000 \text{ K}$, $\log g = 2.2$, $R_{\star} = 46 R_{\odot}$, $d = 822 \text{ pc}$ (close to 847 pc the HIPPARCOS estimate), and $E(B - V) = 0.10$ (lower than the colour excess of 0.131 mag we obtained from Flower 1996). The calculation of R_{\star} by means of the angular diameter gives $51 R_{\odot}$, while the computed M_{bol} (-8.53 mag) suggests $R_{\star} = 46 R_{\odot}$. We adopted $R_{\star} = 46 R_{\odot}$.

The photospheric lines are broadened by macroturbulent motion ($V_{\text{macro}} = 60 \text{ km s}^{-1}$). This high value of V_{macro} , which is almost twice the measured value for the projected rotation ve-

locity, is consistent with the suggestion of a pulsating variable star of α Cyg type (Lefèvre et al. 2009).

Our model fits the observed He I $\lambda 4471$ Å line and the emission component of H α fairly well, although we were not able to reproduce the absorption component of the profile in 2006 or the emission component observed in 2013. Our mass-loss estimates are in the range of previously determined values of other authors, being higher in 2006. The terminal velocity measured in the spectrum of 2013 is lower than in 2006 (see Table A.1). Barlow & Cohen (1977) measured a significant infrared excess at 10 μ m requiring a mass-loss rate a factor of 20 times higher than ours to account for it.

HD 58350 (B5Ia) is an MK standard star. The set of stellar parameters derived with FASTWIND ($\log g$ and T_{eff}) agree very well with those derived by McErlean et al. (1999); Searle et al. (2008); Fraser et al. (2010). We were not been able to obtain a good fit to the SED using simultaneously the UV, visual, and IR photometry. However, based on the distance given by HIPPARCOS (609 pc) and the calculated angular diameter (0.882 mas, Zorec et al. 2009), we obtained $R_{\star} = 57 R_{\odot}$. Based on HIPPARCOS parallax measurement and the derived $E(B - V) = 0.083$ mag from Flower (1996), we obtained $M_{\text{bol}} = -7.97$ mag and $R_{\star} = 51 R_{\odot}$. We adopted $R_{\star} = 54 R_{\odot}$ as the mean value.

The H α line shows a variable P Cygni profile with a tiny emission component. We were able to match the observations taken in 2006 and to get a fairly good fit to the one acquired in 2013. In the former, we failed to fit the absorption component. Our mass-loss rate is similar to that given by Lefever et al. (2007) and lower than the value given by Searle et al. (2008). As these last authors do not show the stellar spectrum in the H α region, we cannot discuss the origin of the discrepancies. Morel et al. (2004) show time-series of the H α line where the profile is seen in absorption, while the observations of Ebbets (1982) display a P Cygni profile. The light curve presents one period of 4.70 days (Koen & Eyer 2002) and another one of 6.631 days (Lefever et al. 2007).

HD 64760 (B0.5Ib) is a rapid rotator. The star was extensively studied as part of the IUE ‘MEGA Campaign’ by Massa et al. (1995) and Prinja et al. (1995). The line variability observed in the UV argues in favour of rotationally modulated wind variations. It displays a double-peaked emission line profile in H α and very broad absorption lines of H and He. Direct observations reveal a connection between multi-periodic non-radial pulsations (NRPs) in the photosphere and spatially structured winds (Kaufer et al. 2006). These observations also seem to be compatible with the presence of co-rotating interaction regions.

The fitting of the SED provides the following parameters: $T_{\text{eff}} = 22\,370$ K, $\log g = 2.50$, $R_{\star} = 15 R_{\odot}$, $E(B - V) = 0.07$ mag, and $d = 486$ pc (while HIPPARCOS parallax gives $d = 507$ pc). The derived $M_{\text{bol}} = -6.72$ mag gives $R_{\star} = 12 R_{\odot}$, while the angular diameter leads to $R_{\star} = 10 R_{\odot}$. We adopted $R_{\star} = 12 R_{\odot}$ as the mean value.

Our stellar parameters derived with FASTWIND ($T_{\text{eff}} = 23\,000$ K, $\log g = 2.90$) agree fairly well with those of Lefever et al. (2007), but show large discrepancies with the values reported by Searle et al. (2008). Although Searle et al. (2008) do not show the spectrum, they mentioned some difficulties in deriving accurate values from the models due to the large width of the spectral lines.

In general, we obtained very good fits for all the lines, even for the double-peaked H α profile. Our model gives the same set of wind parameters as Lefever et al. (2007), but for the stellar

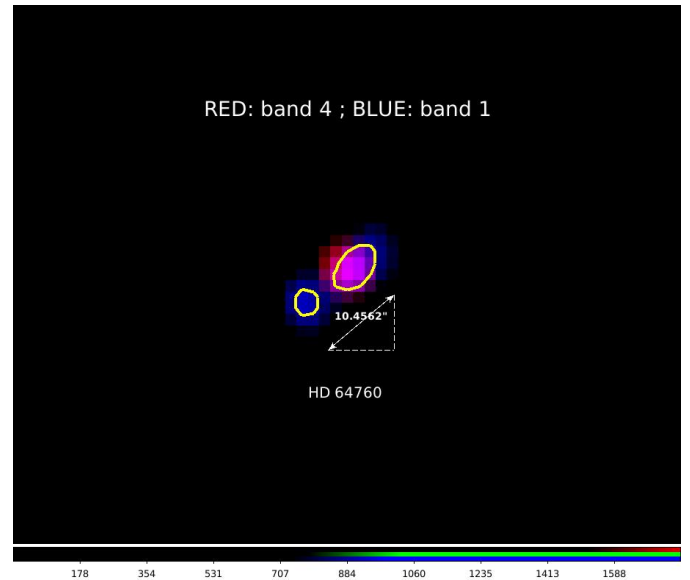


Fig. 3. WISE W1 and W4 images (3.4 μ m and 22 μ m, respectively) showing a double component or a wind-lobe structure. Yellow curves represent regions with the same brightness.

radius a half of the value published by these authors was obtained. The combined WISE W1 and W4 images (3.4 μ m and 22 μ m, respectively) show the presence of either a double visual component or a wind-lobe structure (see Fig. 3).

HD 74371 (B6Iab/b) displays light variations with periods of 5 – 20 days (van Genderen et al. 1989) and 8.291 days (Koen & Eyer 2002; Lefèvre et al. 2009). The stellar parameters T_{eff} and $\log g$ were determined by Fraser et al. (2010) and agree very well with the values that we derived with FASTWIND ($T_{\text{eff}} = 13\,700$ K, $\log g = 1.8$). From the SED we were not able to get a good fit using the HIPPARCOS parallax (0.43 mas, $d = 2.3$ kpc van Leeuwen 2007). The best fit was achieved using a distance of 1.8 kpc, $E(B - V) = 0.35$, $T_{\text{eff}} = 13\,800$ K, $\log g = 2.0$, and $R_{\star} = 73 R_{\odot}$. The found distance of 1.8 kpc agrees with the value reported by Humphreys (1978, 1.9 kpc).

Our model fits all the lines very well, with the exception of the absorption component of the H α P Cygni profile and the core of the H β line, which seems to be filled in by an incipient emission (Fig. A.4). This is the first time that the wind parameters of HD 74371 have been determined (see Table 3).

HD 75149 (B3Ia): The stellar parameters obtained in this work with FASTWIND agree very well with those given by Lefever et al. (2007), Fraser et al. (2010), and our SED model with $T_{\text{eff}} = 15\,000$ K, $\log g = 2.12$, $R_{\star} = 71 R_{\odot}$, $E(B - V) = 0.46$ mag, and a distance of 1 642 pc. We were not able to fit the SED with the parallax measurement of 0.37 mas (2.7 kpc) given by HIPPARCOS, but our value of d is within the corresponding error bars (1.4 kpc). The derived distance of 1.64 kpc leads to $M_V = -7.05$, which is in agreement with the value calculated by Humphreys (1978, -7.0), $M_{\text{bol}} = -8.45$ and $R_{\star} = 56 R_{\odot}$. The angular diameter also gives $R_{\star} = 58 R_{\odot}$. We adopted a mean value of $R_{\star} = 61 R_{\odot}$. The star displays small amplitude light variations with a period of 1.086 days (Koen & Eyer 2002; Lefèvre et al. 2009), in addition to the variability of 1.2151 days and 2.2143 days reported by Lefever et al. (2007).

From our spectra, we found that the star shows important variations in the H α line: an absorption line profile with a weak emission at the core is seen in 2006. A P Cygni feature is seen

on 2013 February 5; it turns into an absorption profile two days later. In 2014 a P Cygni profile with a complex absorption component is seen again (see Fig. 1); this profile also presents two weak emission components that resemble the one published by Lefever et al. (2007). Using the spectrum taken in 2006 the derived \dot{M} is similar to the value reported by these authors, although our value of V_∞ is a bit lower. To explain the line profile changes we have to assume a variable wind structure with a mass-loss enhancement of a factor of about 1.8 and 2.2, between our observation in 2013 and in 2014, and of a factor of about 2.8, between data taken in 2014 and 2006. We want to stress that in order to model the H α line width at various epochs, it was necessary to consider different and also large values for V_{macro} . The terminal velocity is very similar in all the models. Nevertheless, we have to keep in mind that the values derived from a pure absorption profile are more uncertain since the line is less sensitive to the wind conditions.

We were able to model all the photospheric lines quite well with the exception of the H β line core observed in 2006, which is weaker.

HD 79186 (B5Ia): From the SED we were able to match a TLUSTY model using the following parameters: $T_{\text{eff}} = 15\,000$ K, $\log g = 2.12$, $R_\star = 67 R_\odot$, and $d = 1.42$ kpc, adopting $E(B - V) = 0.35$ mag. The distance is very similar to that obtained from the HIPPARCOS parallax (1.45 kpc), which yields $M_{\text{bol}} = -8.26$ mag and $R_\star = 53 R_\odot$, while the angular diameter (0.4 mas) gives $61 R_\odot$. We used a mean stellar radius of $61 R_\odot$.

Our estimation of T_{eff} is slightly higher than the values given by Fraser et al. (2010) and Prinja & Massa (2010), respectively $\Delta T \sim 700$ K and $\Delta T \sim 800$ K, and even higher than those obtained by Krtićka & Kubát (2001) and Underhill (1984).

The logarithm of the surface gravity agrees with the unique value (2.0 dex) available in the literature (Fraser et al. 2010). The stellar radius of our model is similar to that estimated by Underhill (1984).

Although we obtained a very good fit for all the photospheric lines, we were not able to reproduce the shallow absorption component of the H α P Cygni profile. Nevertheless, the terminal velocity agrees with the model parameters given by Krtićka & Kubát (2001) and with measurements from UV observations (435 km s^{-1} , Prinja & Massa 2010). Our \dot{M} is slightly lower than the value given by Krtićka & Kubát (2001).

HD 80077 (B2Ia+e) might be a member of the open cluster Pismis 11, located at a distance of 3.6 kpc. With an absolute bolometric magnitude of -10.4, this star is among the brightest of the known B-type supergiants in our Galaxy (Knoechel & Moffat 1982; Marco & Negueruela 2009).

Carpay et al. (1989, 1991) detected light variations with an amplitude ~ 0.2 mag and suggested that the star could be a luminous blue variable (LBV). Using HIPPARCOS and V photometric data, van Leeuwen et al. (1998) obtained a periodogram that reveals that the most significant peaks are those near 66.5 days and 55.5 days, and peaks with much lower significance near 76.0 days and 41.4 days.

Light variations of 0.151 mag over a period of 3.115 days were found by Lefèvre et al. (2009) and another period of 21.2 days was determined from the polarimetry (Knoechel & Moffat 1982). From the SED we obtained $T_{\text{eff}} = 18\,000$ K, $\log g = 2.17$, $E(B - V) = 1.5$ mag, $R_\star = 200 R_\odot$, and $d = 3\,600$ pc (while the HIPPARCOS distance is 877 pc). Using the distance to the Pismis 11 cluster and the obtained $E(B - V)$, we calculated M_{bol}

$= -11.49$ mag and $R_\star = 187 R_\odot$. We adopted a stellar radius of $195 R_\odot$.

Carpay et al. (1989) derived $T_{\text{eff}} = 17\,700$ K, $\log g = 2$, and a mass-loss rate of $5.11 \times 10^{-6} M_\odot \text{ yr}^{-1}$. Based on radio data, Benaglia et al. (2007) estimated a significantly lower mass-loss rate ($1.7 \times 10^{-6} M_\odot \text{ yr}^{-1}$) that agrees with our result (see Table A.1). We observed a P Cygni H α profile in the spectra taken in 2006 and 2014. Small changes in the emission and absorption components can be seen in Fig. 1.

Finally, we want to stress that HD 80077 is a very massive post-main sequence star and, hence, an enhancement of the He abundance is expected. However, we do not observe any noticeable contribution of forbidden components and the He I $\lambda 4471$ line was well-matched with a solar He abundance model.

HD 92964 (B2.5Ia) displays photometric variations with periods of 2.119 days and 14.706 days (Lefèvre et al. 2009). The H β and H γ line profiles show asymmetries. Lefever et al. (2007) ascribed this behaviour to the strong stellar wind which affects the photospheric lines. The same authors also noted that the He I $\lambda 6678$ line requires a V_{macro} that is two times higher than the value derived for the Si lines.

The stellar parameters derived from the SED are $T_{\text{eff}} = 18\,000$ K, $\log g = 2.19$, $E(B - V) = 0.481$, $R_\star = 76 R_\odot$, and $d = 1\,806$ pc (close to the HIPPARCOS distance, $d = 1\,851$ pc). We used the extinction curve from van Breda et al. (1974), who found $R = 3.5$ for this star. From the HIPPARCOS distance and the calculated $A_V = 1.68$ mag we obtained $M_{\text{bol}} = -9.14$ mag and $R_\star = 62 R_\odot$, and from the angular diameter (0.37 mas Pasinetti Fracassini et al. 2001) the derived stellar radius is $73 R_\odot$. As a mean value we used $R_\star = 70 R_\odot$.

From our modelling of the photospheric lines, done with FASTWIND, we obtained $T_{\text{eff}} = 18\,000$ K and $\log g = 2.2$. The derived T_{eff} agrees with the values adopted by Lefever et al. (2007) and Krtićka & Kubát (2001), but present large departures from the atmospheric parameters derived by Fraser et al. (2010). To model the spectrum we used a projected rotational velocity (40 km s^{-1}) that is slightly higher than that given in the literature (28 km s^{-1} and 31 km s^{-1}). As did Lefever et al. (2007), we found a very high value for V_{macro} .

Previous observations reveal important intensity variations in both absorption and emission components of the P Cygni profile of the H α line (see Fig. A.1 given in Lefever et al. 2007). Comparing our spectra with that observation, the H α line observed in 2013 shows a wider absorption and a higher emission component. We were able to reproduce only the emission component of the H α line profile. Nevertheless, we derived a value for $V_\infty = 370 \text{ km s}^{-1}$ that is close to that measured using the UV lines (435 km s^{-1} , Prinja et al. 1990) and lower than the values quoted in Table A.1. However, the mass-loss rate obtained in this work is consistent with the value measured by Lefever et al. (2007).

HD 99953 (B1/2 Iab/b) is a poorly studied star. Fraser et al. (2010) derived the following stellar parameters: $T_{\text{eff}} = 16\,800$ K and $\log g = 2.15$. Based on our modelling of the H γ , Si III, and He I lines, we obtained a new set of values: $T_{\text{eff}} = 19\,000$ K and $\log g = 2.30$. The latter are compatible with the assigned spectral classification and the observed SED ($T_{\text{eff}} = 18\,830$ K, $\log g = 2.30$, $E(B - V) = 0.56$, $R_\star = 28 R_\odot$) for $d = 1\,077$ pc (which is similar to the HIPPARCOS distance, 1 075 pc). This distance and $E(B - V)$ predict $M_{\text{bol}} = -7.16$ mag and $R_\star = 22 R_\odot$. We adopted $R_\star = 25 R_\odot$ as the mean value.

The H α line shows a P Cygni profile and its intensity varies with time. The mass-loss and terminal velocity change by a fac-

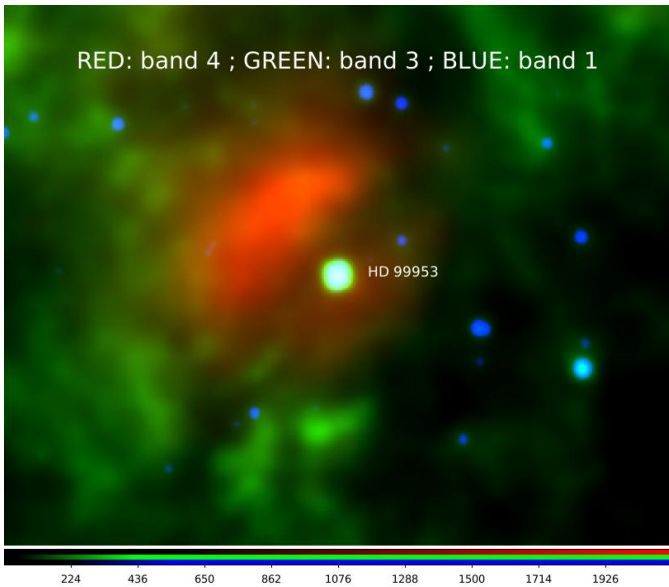


Fig. 4. WISE images showing wind-blown and warm dust structures around HD 99953.

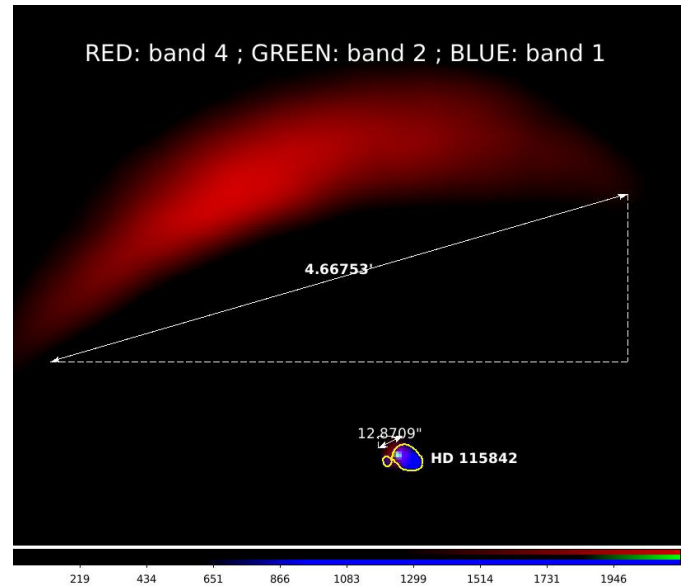


Fig. 5. Bow-shock structure and asymmetric density structure associated with HD 115842. The yellow curves represent regions with the same brightness, each one associated with a different lobe.

tor of ~ 2.8 . Different values of V_{macro} were needed to model the line at different epochs.

This work reports the first determinations of the mass-loss rate of the star ($\dot{M} = 0.08 \cdot 10^{-6} M_{\odot} \text{ yr}^{-1}$, $0.13 \cdot 10^{-6} M_{\odot} \text{ yr}^{-1}$, and $0.22 \cdot 10^{-6} M_{\odot} \text{ yr}^{-1}$). The terminal velocity derived from the $H\alpha$ line ranges from 250 km s^{-1} to 700 km s^{-1} . This wide range includes the value measured from the UV spectral region (510 km s^{-1} , Prinja et al. 1990). The combined WISE W3 and W4 images show warm dust heated by radiation coming from the star (see Fig. 4).

HD 111973 (B2/3Ia): This spectroscopic binary was classified as a B3 I star (Chini et al. 2012). It presents light variations with periods of 57.11 days and 9.536 days (Koen & Eyer 2002).

The SED was fitted with a TLUSTY model with $T_{\text{eff}} = 17180 \text{ K}$, $\log g = 2.18$, $R_{\star} = 48.6 R_{\odot}$, $E(B - V) = 0.38 \text{ mag}$, and $d = 1660 \text{ pc}$. The colour excess was obtained with the calibration scale of Flower (1996). Using this distance and the derived colour excess, we obtained $M_{\text{bol}} = -7.81 \text{ mag}$ and $R_{\star} = 40 R_{\odot}$. On the other hand, when using the angular distance (0.26 mas) we have $R_{\star} = 46 R_{\odot}$, a value that is close to that derived by Pasinetti Fracassini et al. (2001, 47 R_{\odot}). We adopted $R_{\star} = 46 R_{\odot}$.

We were able to match all the photospheric lines. The derived T_{eff} and $\log g$ (16500 K and 2.1 dex) are similar to those reported by Fraser et al. (2010, 16000 K and 2.3 dex) and Prinja & Massa (2010, 16500 K).

The $H\alpha$ line shows short-term variations: we observed a P Cygni profile with a weak emission component that turned into an absorption profile the following night (see Fig. 1). This variation is similar to the expected dynamical timescale of a prototypical BSG wind (~ 1.3 days). We modelled the $H\alpha$ line and derived a lower terminal velocity than the value measured from the UV lines (520 km s^{-1} Prinja & Massa 2010). Furthermore, a high $V_{\text{macro}} = 160\text{--}190 \text{ km s}^{-1}$ was needed to model this line.

This work reports the mass-loss rate of the star for the first time. It ranges from $0.14 \cdot 10^{-6} M_{\odot} \text{ yr}^{-1}$ to $0.21 \cdot 10^{-6} M_{\odot} \text{ yr}^{-1}$.

HD 115842 (B0.5Ia/ab) presents photometric variations on a timescale of 13.38 days (Koen & Eyer 2002) and variations in

the $H\alpha$ line profile. Our spectrum displays the $H\alpha$ line in pure emission (see Fig. 1), while the one given by Crowther et al. (2006) displayed a P Cygni feature. The $H\beta$ line is seen in absorption and the profile is slightly asymmetric (see Fig. A.7).

From the SED we derived the following parameters: $T_{\text{eff}} = 25830 \text{ K}$, $\log g = 2.73$, $R_{\star} = 38 R_{\odot}$, $E(B - V) = 0.6 \text{ mag}$, and $d = 1543 \text{ pc}$. This colour excess fits the observed 2200 \AA bump feature and is higher than the $E(B - V) = 0.53 \text{ mag}$ derived from Flower (1996). The obtained distance is consistent with the HIPPARCOS and Gaia parallaxes (0.65 mas and 0.6105 mas, respectively) and the distance of 1583 pc estimated from the Ca II H and K lines (Megier et al. 2009). Using the HIPPARCOS distance (1538 pc) and $E(B - V) = 0.6 \text{ mag}$, we calculated $M_{\text{bol}} = -9.22 \text{ mag}$ and $R_{\star} = 32 R_{\odot}$, while from the angular diameter (0.22 mas, Pasinetti Fracassini et al. 2001) we derived $R_{\star} = 33 R_{\odot}$. We adopted $R_{\star} = 35 R_{\odot}$ as the mean value.

We achieved very good fits to the photospheric lines for $T_{\text{eff}} = 25500 \text{ K}$ and $\log g = 2.75$. The stellar parameters derived in this work agree with those found by Crowther et al. (2006) and Fraser et al. (2010) (see Table A.1). We obtained a lower mass-loss rate ($1.8 \cdot 10^{-6} M_{\odot} \text{ yr}^{-1}$) and a higher terminal velocity (1700 km s^{-1}) than the Crowther et al. (2006) estimates ($2.0 \cdot 10^{-6} M_{\odot} \text{ yr}^{-1}$, 1180 km s^{-1}).

Our value of V_{∞} is also higher than the value determined from the IUE data (1125 km s^{-1} , Evans et al. 2004). These authors reported a very high macroturbulence, $V_{\text{macro}} = 225 \text{ km s}^{-1}$, which is twice our estimate.

WISE W3 and W4 images show a large well-defined bow-shock structure (see Fig. 5) related to a possible strong wind-ISM interaction phase. In addition, an asymmetric density structure seems to be present in the WISE W1 image with an angular size that is greater than the WISE resolution.

HD 148688 (B1Iaeqp) is a southern oxygen-rich supergiant that displays line variations (Jaschek & Brandi 1973). Data from the HIPPARCOS satellite correlate with periods of 1.845 days and 6.329 days (Lefever et al. 2007).

The best-fitting model to the observed SED leads to $T_{\text{eff}} = 20650 \text{ K}$, $\log g = 2.2$, $R_{\star} = 34 R_{\odot}$, and $d = 838 \text{ pc}$ (while the

HIPPARCOS distance is 833 pc). This gives $M_{\text{bol}} = -7.97$ mag and $R_{\star} = 26 R_{\odot}$, for $E(B - V) = 0.54$ mag. This $E(B - V)$ was obtained from Flower (1996) and also fits the deep bump at 2 200 Å present in the SED. We adopted $R_{\star} = 31 R_{\odot}$ as the mean value.

The stellar parameters obtained from FASTWIND ($T_{\text{eff}} = 21\,000$ K and $\log g = 2.45$) are in better agreement with the works of Fraser et al. (2010) and Lefever et al. (2007). The H α line from Fig. 1 shows a P Cygni feature that looks like the one shown by Lefever et al. (2007), while the spectrum of Crowther et al. (2006) exhibits an emission line.

We were only able to model the emission component of the P Cygni profile. We obtained a mass-loss rate that is a factor of 1.1 and 1.4 lower than the values found by Lefever et al. (2007) and Crowther et al. (2006), respectively. The terminal velocity is similar to the value found by Lefever et al. (2007, see Table A.1), although it is greater than measurements derived from the UV lines (725 km s⁻¹, Prinja et al. 1990).

4.2. Global properties of stellar and wind parameters

Although the stars present spectral variability, it is still possible to describe their global properties. Figure 6 shows a comparison of T_{eff} of BSGs with the spectral subtype. The sample is a collection of data from the literature and this work. With the exception of those stars that have T_{eff} based on the BCD spectrophotometric calibration (Zorec et al. 2009), the effective temperature was obtained via adjustments of the line profiles of He I, He II, and line intensity ratio of Si IV/Si III or Si III/Si II, as in this work.

We performed a fit to the observed T_{eff} versus spectral subtype relation using a third-order polynomial regression ($a = -54.6 \pm 7.7$, $b = 973.4 \pm 107.5$, $c = -6054.3 \pm 387.9$, and $d = 27316 \pm 331$). The derived coefficients agree very well with the fit obtained by Markova & Puls (2008). We illustrate our fit in Fig. 6 with a grey wide band that has a dispersion of 1 290 K. The supergiants of our sample, with the exception of HD 52089, HD 53138, and HD 47240 (indicated in the figure with large open circles), fall inside the traced relation. Moreover, we can observe that the departures of the effective temperatures for the early BSGs range roughly from 0 K to 5 000 K and tend to be lower the later the B spectral subtype. This same tendency is also observed in Markova et al. (2008).

Figure 7 displays a linear correlation between $\log T_{\text{eff}}$ and $\log g_{\text{cor}}$ (the surface gravity corrected by the centrifugal acceleration, see Table A.1). This kind of correlation was previously reported by Searle et al. (2008). We performed a linear fit and obtained a slope of 3.98 ± 0.31 . This indicates that most of the stars in our sample have a similar luminosity-to-mass ratio ($\log(L/M) \sim 4$), as expected, since $L \propto T_{\text{eff}}^4$.

A large scatter is observed around the stars that have large $\log g_{\text{cor}} (\geq 2.5)$; in particular HD 42087, HD 52089, and HD 64760 do not follow the relation. Two of these stars, HD 42087 and HD 64760, are close to the TAMS so we believe they have just left the main sequence. HD 64760 is a high rotator and, as a consequence, we should observe higher apparent bolometric luminosities and lower effective temperatures than those expected for their non-rotating stellar counterparts (Frémat et al. 2005; Zorec et al. 2005), giving a later evolutionary stage of the object.

From Table 3 we can distinguish stars showing two different wind regimes. One group gathers stars with steep velocity gradients, $\beta \leq 1$, in good agreement with the standard wind theory, while the other group shows values of β between 1.5 and 3.3, similar to the results reported by Crowther et al. (2006); Searle

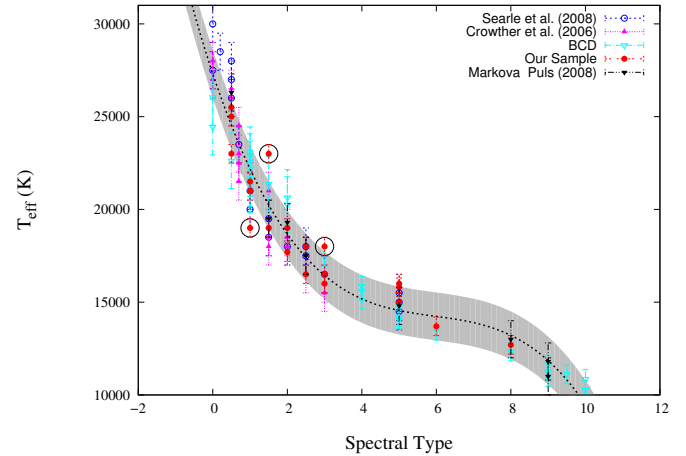


Fig. 6. Effective temperature as function of the spectral subtype. The relation was fitted using a third-order polynomial regression (dotted line) with a dispersion of 1 290 K (grey band, see text for details). Comparison of our sample of Galactic B supergiants with a set of BSGs collected from the literature. Data points of our sample with large open circles are outliers.

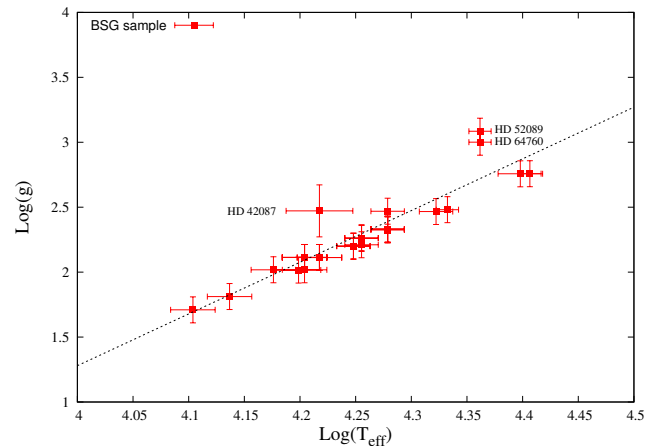


Fig. 7. Linear relation ($\log T_{\text{eff}} - \log g_{\text{cor}}$) of our sample of B Galactic supergiants (dashed line). The surface gravity was corrected by the centrifugal acceleration.

et al. (2008), and Markova et al. (2008). Stars with β between 2 and 2.5 are the most common ones. High values of β are often found among the late B-type stars.

The terminal velocities range from 155 km s⁻¹ to 1 700 km s⁻¹, while mass-loss rates range generally from $0.08 \times 10^{-6} M_{\odot} \text{ yr}^{-1}$ to $0.7 \times 10^{-6} M_{\odot} \text{ yr}^{-1}$ (four stars fall outside this mass-loss range).

In addition, we calculate the average values for the total mechanical momentum flow of the wind, D_{mom} , as a function of the luminosity of the star. This is known as the modified WLR (Kudritzki et al. 1995), given by

$$D_{\text{mom}} = \dot{M} v_{\infty} R^{0.5} \propto L^{1/\alpha_{\text{eff}}}, \quad (1)$$

where $\alpha_{\text{eff}} = \alpha - \delta$ (see details in Kudritzki et al. 1999; Puls et al. 1996); α and δ are the force multipliers related to the line opacity and wind ionization, respectively.

Our sample splits into two different groups (see Fig. 8): the early BSGs with spectral types between B0 and B1.5 (blue diamonds) and mid- to late-type BSGs with spectral types from B2

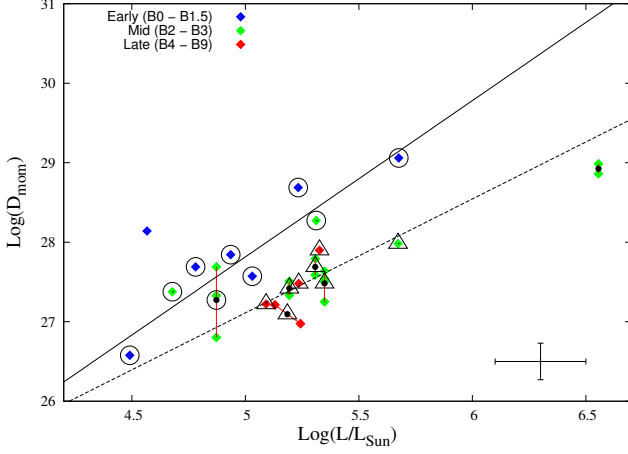


Fig. 8. Wind-momentum luminosity relationships (dotted lines). Blue, green, and red diamonds represent early-, mid-, and late-type BSGs, respectively. The upper fit line was derived using data points in large circles, while the lower fit line corresponds to data points with large triangles. Diamond symbols connected with solid lines correspond to observations of the same star in different epoch (black dots represent their average values).

to B9 (green and red diamonds). These two groups seem to be clearly separated. However, among the early B supergiants we found three mid B stars (HD 41117, HD 42087, and the variable star HD 99953) with wind momentum rates comparable to the early ones.

From a linear regression, we found that the sample of the early BSGs plus the three mentioned mid B stars (see Fig. 8, large circles) can be fitted by the following relationship:

$$\log D_{\text{mom}} = 1.96(\pm 0.28) \log L/L_{\odot} + 17.98(\pm 1.43), \text{ for B0} - \text{B1.5.} \quad (2)$$

The second WLR was traced using BSG stars with spectral types B2-B9 (see Fig. 8, large triangles). The values of the wind momentum rates of these stars are clearly lower than those of the early-type objects. Furthermore, the WLR displays a different slope (less steep) with luminosity. For these objects we find a linear regression of the form

$$\log D_{\text{mom}} = 1.43(\pm 0.42) \log L/L_{\odot} + 19.94(\pm 2.23), \text{ for B2} - \text{B9.} \quad (3)$$

The observed offset between the WLRs increases from the early- to the mid-type BSGs. Despite the large errors of these quantities, the tendency is opposite to the results observed by Kudritzki et al. (1999) and predicted by Vink (2000).

In Fig. 8, observations of the same star at different epochs are connected by solid lines. For these stars, average values of $\log D_{\text{mom}}$ (Fig. 8, black dots) were considered to fit the regression line of the WLR for each group, i.e. early B or mid/late B stars. In the next section, we return to the issue of mass-loss variations.

It is interesting to stress that the wind regime of the stars defining each WLR is different. From Table 3 we found that the early-type stars have mostly $\beta \lesssim 2$ and terminal velocities greater than 500 km s^{-1} , while the mid- and late-type stars have $\beta \geq 2$ and terminal velocities lower than 500 km s^{-1} .

On the other hand, the parameter α_{eff} , which is the inverse of the slope of the WLR, changes from 0.5 for the early BSGs

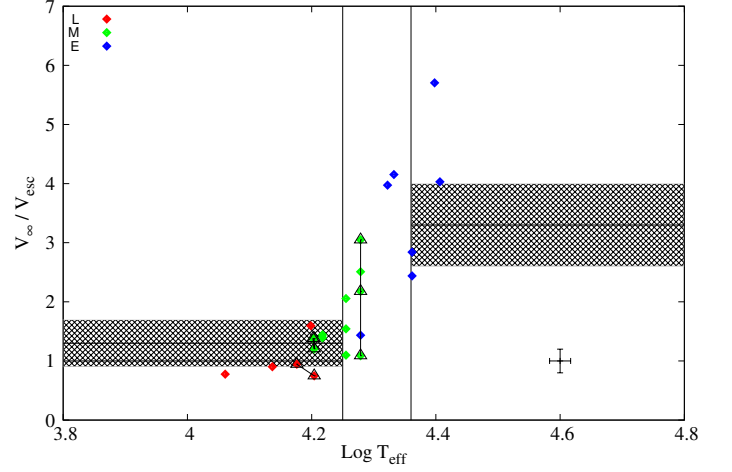


Fig. 9. Ratios of $V_{\infty}/V_{\text{esc}}$ as a function of $\log T_{\text{eff}}$. Early-type (E), mid-type (M), and late-type (L) stars are indicated by blue, green, and red diamonds, respectively. Stars with wind variability are indicated with large open triangles and connected with a solid line. The largest variability is shown by HD 99953, which is located in the region limited by vertical black lines (the bi-stability jump). The shaded areas refer to two zones with different $V_{\infty}/V_{\text{esc}}$: 3.3 for effective temperatures above 23 000 K, and 1.3 below 18 000 K, with errors of 43% and 33%, respectively, which were identified by Markova & Puls (2008).

to 0.7 for the mid/late ones. An increase in α_{eff} might suggest highly structured ionized outflows that lead to a weakening of the radiation force. Under this condition, different mechanisms (e.g. pulsations, clumping) might also contribute to driving the wind.

Finally, Fig. 9 shows the ratios of $V_{\infty}/V_{\text{esc}}$ as a function of $\log T_{\text{eff}}$. In the figure we present our results together with the two temperature regions defined by Markova & Puls (2008), which show significantly different $V_{\infty}/V_{\text{esc}}$ ratios: 3.3 for effective temperatures above 23 000 K, and 1.3 below 18 000 K. Errors of 33% for the cooler and 43% for the hotter regions are shown as shaded areas (for details on the error determinations, see Markova & Puls 2008).

The region in between, delimited by vertical black lines, is called the bi-stability jump. Markova & Puls (2008) showed that the stars located there show a gradual decrease in $V_{\infty}/V_{\text{esc}}$. Overall, our results show a similar behaviour to that reported by these authors. In particular, we found many stars in our sample located inside the bi-stability region. Moreover, as some stars are variable we also plotted in Fig. 9 the various positions of those stars observed during different epochs. These positions are connected with a solid black line.

The variation in $V_{\infty}/V_{\text{esc}}$ of those stars on the cool side of the bi-stability jump seems to be small. Instead, HD 99953 (green diamonds with triangles), which is located inside the bi-stability region, presents such a large wind variability that it seems to switch from a slow to a fast regime. The same variation for this star is observed in the WLR. With the exception of HD 80077, which has a huge mass-loss rate, we do not observe that a decrease in $V_{\infty}/V_{\text{esc}}$ is accompanied by an increase in the mass-loss rate, as predicted by Vink et al. (1999). In general, mid and late BSGs present values of \dot{M} that are similar to or lower than those of the stars located on the hot side of the bi-stability jump.

5. Discussion

5.1. Photospheric parameters

For some stars different estimates of T_{eff} and $\log g$ ($\Delta T_{\text{eff}} > 1500$ K, and $\Delta \log g \sim 0.2$) are found in the literature (see Table A.1).

In relation with these T_{eff} estimates, it is important to point out that this parameter is derived using different methods or approaches. Quite often the atmospheric parameters are obtained by fitting the observed line profiles with a synthetic spectrum calculated from NLTE line-blanketed plane-parallel hydrostatic model atmospheres, using the codes TLUSTY and SYNSPEC (Hubeny & Lanz 1995; Lanz & Hubeny 2007). This procedure was mainly carried out by Fraser et al. (2010); McErlean et al. (1999); Kudritzki et al. (1999), while Crowther et al. (2006); Lefever et al. (2007); Markova & Puls (2008); Searle et al. (2008) used codes like FASTWIND or CMFGEN (Puls et al. 2005; Hillier & Miller 1998) that solve multi-level non-LTE radiative transfer problems in the co-moving frame, based on NLTE line-blanketed spherically symmetric wind models.

For most of the stars in our sample, we found good agreement between our T_{eff} estimates and those obtained by Crowther et al. (2006, six stars in common), Lefever et al. (2007, eight stars in common), and Searle et al. (2008, five stars in common), within error margins of ± 1500 K. Good agreements were also found with the values derived by Fraser et al. (2010, twelve stars in common), who used TLUSTY. Among all the previous mentioned authors, the largest discrepancies in T_{eff} are found for six stars, HD 42087, HD 52089, HD 53138, HD 64740, HD 92964, and HD 99953, which show appreciable differences ($\Delta T_{\text{eff}} > 2000$ K). Two of them (HD 53138 and HD 64740) have shown either some degree of ion stratification or ionization changes in the UV lines (see details in Prinja et al. 2002). The star HD 52089 has a magnetic field and X-ray emission (see section 4.1) and like HD 99953 is located inside the bi-stability region. This might suggest that these stars show intrinsic temperature variations since we do not observe a tendency regarding a particular method used to derive their atmospheric parameters.

We also found that the line spectra do not show He forbidden components suggesting that the He abundance is close to the solar value. This is in accordance with what Kraus et al. (2015) observed in 55 Cyg. In addition, Crowther et al. (2006) did not report any discrepancies on the Si and He abundances.

We did not find any correlation between V_{macro} and T_{eff} , as was reported by Fraser et al. (2010). In general, we needed larger values for V_{macro} (mostly around 50 – 60 km s⁻¹ for all the stars) than the ones given in the literature to be able to fit the photospheric line widths. In some cases it was even necessary to slightly increase $V \sin i$ as well. This could be due to our use of a mean value for V_{macro} to model all the lines and, particularly, the line-forming region for He might extend into the base of the wind where higher turbulent velocities can be expected.

The major discrepancy found among the stellar parameters with previous works is related to the determination of the stellar radius, due to the different methods used to calculate distances to stars. We think that the values we estimated in section §4.1 are quite reliable. Uncertainties in the stellar radius yield an insecure luminosity and a mass-loss discrepancy. This last issue is discussed in the next subsection.

5.2. Spectral and wind variability

Variable B supergiants often show spectroscopic variability in the optical and UV spectral region that can be attributed to the large-scale wind structures (Prinja et al. 2002). Variations linked to rotational modulation have been reported, for example, in HD 14134 and HD 64760 (Morel et al. 2004; Prinja et al. 2002, respectively), while those associated with pulsation activity were found in HD 50064 and 55 Cyg (Aerts et al. 2010; Kraus et al. 2015, respectively). Nevertheless, variability related to the presence of weak magnetic fields has also been proposed (Henrichs et al. 2003; Morel et al. 2004).

Most of the stars in our sample show H α line variations in both shape and intensity. These variations can take place on a scale of a few days, but daily and even hourly variability has also been reported (e.g. Morel et al. 2004; Kraus et al. 2012, 2015; Tomić et al. 2015). Among our sample, HD 75149, HD 53138, and HD 111973 display emission-line episodes or dramatic line profile variations with a diversity of alternating shapes (from a pure absorption to a P Cygni profile and vice versa).

Regarding the amplitude of the mass-loss variation in individual objects, Prinja & Howarth (1986) measured a variability at 10% level on timescales of a day or longer, while Lefever et al. (2007) and Kraus et al. (2015) reported on ratios between maximum and minimum mass-loss rates ranging from 1.05 up to 2.5.

In this way, based on a carefully study of the variation in the H α line among the stars we observed at different epochs (modelled with the code FASTWIND), the largest variations in \dot{M} (a factor of 1.5 to 2.7) are detected in HD 75149, HD 99953, and HD 111973. As the H α line is very sensitive to changes in the mass density and in the velocity gradients at the base of the wind (Cidale & Ringuet 1993), a connection between line variability and changes in the wind structure due to photospheric instabilities can be expected.

To gain insight into the origin of the variability of the BSG winds, we gathered information from the literature for all our objects on periods of light and spectroscopic variations (quoted in Table 1), and on previous determinations of the wind parameters derived from individual modelling attempts. A comparison of the mass-loss estimates listed in Table A.1 is of particular interest as they display ratios between maximum and minimum values that range from 1 to 7. These discrepancies are not completely true because these models were computed using different stellar radii, and the differences in mass-loss rates could be much lower. For instance, for HD 34085 we found a discrepancy in \dot{M} of 1.9 when compared with the result given by Markova & Puls (2008), but it could be only 1.3 times higher ($\dot{M} = 0.44 \times 10^{-6} M_{\odot} \text{ yr}^{-1}$) if a value of $R_{\star} = 115 R_{\odot}$ is adopted (keeping all the other parameters constant).

Therefore, to compare the values obtained by different authors we should discuss the scaling properties of the corresponding models since line fits are not unique (Puls et al. 2008). Thus we will adopt the optical-depth invariant $Q_r = \dot{M}/R_{\star}^{1.5}$, instead of the traditional parameter $Q = \dot{M}/(R_{\star} V_{\infty})^{1.5}$ (Puls et al. 1996) since we assume that V_{∞} can change due to the wind variability. The corresponding calculations and errors for $\log Q_r$ are given in Table A.1. An overview of these values shows that the differences in $\log Q_r$ (for the stars we observed at different epochs) are two or three times larger than their corresponding error bars suggesting real variations in the wind parameters. These differences can also be observed among the Q_r values we calculated from data given by different authors.

It is interesting to note that we found five stars in the domain of the bi-stability region. HD 99953 shows pronounced H α vari-

ations from which different estimations of V_∞ (250 km s⁻¹, 500 km s⁻¹, and 700 km s⁻¹) and \dot{M} ($0.08 \times 10^{-6} M_\odot \text{ yr}^{-1}$, $0.13 \times 10^{-6} M_\odot \text{ yr}^{-1}$, and $0.22 \times 10^{-6} M_\odot \text{ yr}^{-1}$) were obtained. This implies variations in V_∞ and \dot{M} of a factor of about 2.8. This result goes against the theoretical prediction made by Vink et al. (1999) who argue that the jump in mass loss is accompanied by a steep decrease in the ratio V_∞/V_{esc} (from 2.6 to 1.3), which is close to the observed bi-stability jump in the terminal velocity. Moreover, these authors proposed that if the wind momentum $\dot{M} V_\infty$ were about constant across the bi-stability jump, the mass-loss rate would have increased by a factor of two from stars with spectral types earlier than B1 to later than B1.

In the particular case of HD 99953, our result indicates that $\dot{M} V_\infty$ is not constant (see Figure 8) nor does the mass loss increase when the ratio V_∞/V_{esc} decreases, even when the observed changes in the variables are of the order of the expected values (~ 2.8). On the other hand, the mass loss derived for HD 99953 ($\log \dot{M} = -6.66$, when $V_\infty = 700 \text{ km s}^{-1}$) agrees with the value computed by Vink et al. (1999, -6.54 for $V_\infty/V_{\text{esc}} = 2.6$) in Table 1; however, the terminal velocity we derived is the half of the theoretical value found by these authors. We do not believe that the discrepancy could be due to the luminosity of the star ($\log L/L_\odot = 4.87 \pm 0.37$) since the models were computed for a $\log L/L_\odot = 5$. We also found that this is not related to the velocity law adopted for the model since HD 47240 does not fit either.

Looking for other observed BSGs with $\log L/L_\odot \sim 5$ (see Table 1), we found that the wind parameters of the stars on the hot side of the bi-stability jump, like HD 38771 (with $\log \dot{M} = -6.85$ and $V_\infty = 1500 \text{ km s}^{-1}$) and HD 52382 (with $\log \dot{M} = -6.62$ and $V_\infty = 1000 \text{ km s}^{-1}$), resemble those listed in Table 1 by Vink et al. (1999). In contrast, the wind parameters of the stars on the cool side of the bi-stability jump, like HD 34085 (with $\log \dot{M} = -6.64$ and $V_\infty/V_{\text{esc}} = 0.8$), HD 58350 (with $\log \dot{M} = -6.82$ and $V_\infty/V_{\text{esc}} = 0.9$), and HD 111973 (with $\log \dot{M}$ between -6.7 and -6.85 , and $V_\infty/V_{\text{esc}} = 1.4$) do not fit any model predictions. They often have lower terminal velocities and mass-loss rates than values expected from the models. This means that a decrease in the ratio V_∞/V_{esc} , both inside and on the cool side of the bi-stability jump, is not accompanied by an increase in the mass-loss rate. This result supports the conclusions drawn by Markova & Puls (2008) who used the modified optical depth invariant and found that both \dot{M} and V_∞ are decreasing in parallel.

We believe that the decrease in both the mass-loss rate and the terminal velocity, on the cool side of the bi-stability jump, could be explained with the δ – *slow* hydrodynamic solution for radiation line-driven winds (Curé et al. 2011). Venero et al. (2016) found that a change in the ionization of the wind, characterized by the parameter δ of the line-force multiplier (Abbott 1982), defines two different stationary wind regimes (fast and slow). The fast regime is always present at high effective temperatures ($> 25\,000 \text{ K}$), while fast or slow regimes could develop at low effective temperatures. Both wind regimes are separated by an instability zone where non-stationary flow regimes exist. Venero et al. (2016) proposed that an initial density perturbation could trigger a switch in the wind regime between fast and slow solutions (and vice versa) in the B mid-type supergiants. In the same work the authors show preliminary computations of wind hydrodynamics using time-dependent wind solutions that lead to the formation of kink velocity field structures which might be related to the evolution of absorption components like the ones observed in the UV line spectrum (DACs). In addition, at temperatures $< 17\,000 \text{ K}$ the models predict a decrease in both ter-

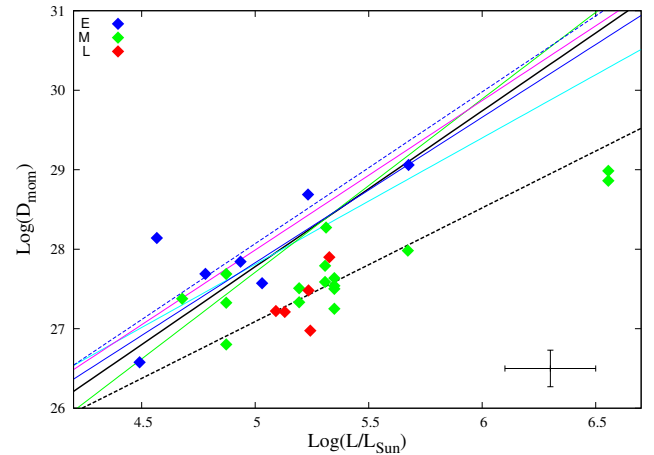


Fig. 10. Comparison of various empirical WLR: this work (solid and dashed black lines are for early BSGs and mid- or late-type BSGs, respectively), Herrero et al. (2002, solid green line), Searle et al. (2008, solid cyan line), and Mokieim et al. (2007, magenta solid line). The theoretical WLR of Vink (2000) is in blue, solid and dashed lines are for $T_{\text{eff}} > 27\,500 \text{ K}$ and $T_{\text{eff}} < 22\,500 \text{ K}$, respectively. The figure includes the sample of stars shown in Fig. 8.

mal velocity and mass-loss rate (see Figure 4 in Venero et al. 2016). Further research on the slow hydrodynamics solution is in progress (Venero et al. 2017).

5.3. The wind momentum–luminosity relationship

The empirical WLR of massive stars is generally represented by a linear regression of the form

$$\log D_{\text{mom}} = X \log L/L_\odot + D_0. \quad (4)$$

Values for the coefficients $X = 1/\alpha_{\text{eff}}$ and D_0 reported in the literature are given in Table 4, together with the parameter α_{eff} and the corresponding errors. It is worth mentioning that previous investigations on the WLR for Galactic BSGs (see Table 4) show that wind momentum rates derived by means of line-blanketed analyses are systematically higher than those reported by Kudritzki et al. (1999).

The coefficients (X , D_0) derived in this work for the early BSGs are close to those obtained by Herrero et al. (2002) and Mokieim et al. (2007), who used a sample of stars consisting mostly of OSGs. Both coefficients also agree with the theoretically predicted values of Vink (2000), but disagree with the values obtained by Kudritzki et al. (1999) and Searle et al. (2008). These relations are plotted in Fig. 10.

Particularly, we find that the difference between our (X , D_0) values and those of Searle et al. (2008) could be due to the fact that the sample of stars selected by these authors considered a mix of early and mid BSG types. In fact, if we split their sample, we obtain $X = 1.85 \pm 0.36$ and $D_0 = 18.47 \pm 2.00$ for early BSGs, and $X = 1.35 \pm 0.14$ and $D_0 = 21.08 \pm 0.73$ for the mid BSGs, which both agree with our values.

5.4. The pulsation–mass-loss relationship

Saio (2011) demonstrated that one or more radial strange modes are expected to be excited in evolved BSGs. These authors computed the periods of excited modes during the evolution of only two stellar models: stars with initial masses of $20 M_\odot$ and $25 M_\odot$.

Table 4. Coefficient for the WLR derived by different authors.

Reference	X	D_0	α_{eff}	sample used
Kudritzki et al. (1999)	1.34 ± 0.25	21.24 ± 1.38		E
Kudritzki et al. (1999)	1.95 ± 0.2	17.07 ± 1.05		M
Vink (2000)	1.826 ± 0.044	18.68 ± 0.26		$T_{\text{eff}} > 22.5$ kK from theory
Vink (2000)	1.914 ± 0.043	18.52 ± 0.23		$T_{\text{eff}} < 27.5$ kK from theory
Herrero et al. (2002)	2.18 ± 0.21	16.81 ± 1.16	0.46 ± 0.04	mostly OSGs
Mokiem et al. (2007)	1.84 ± 0.17	18.87 ± 0.98	0.54 ± 0.05	mostly OSGs
Searle et al. (2008)	$1.59 \pm$	19.86 ± 0.78	0.63 ± 0.06	E & M
This work	1.96 ± 0.28	17.98 ± 1.43	0.51 ± 0.07	E
This work	1.43 ± 0.42	19.94 ± 2.23	0.70 ± 0.21	M & L

Notes. E, M, and L refer to early-, mid-, and late-type B supergiants.

It appears that the periods of these radial strange modes tend to decrease when the effective temperature of the star increases during the blue-ward evolution.

As radial strange modes are considered suitable to trigger mass loss, we first checked which of the known (photometric and spectroscopic) periods (see Table 1) might be considered as radial strange modes, and then opted for a comparison of these periods with the amplitude of the mass-loss rates (i.e. ratios between maximum and minimum values) using the Q_r parameters given in Table A.1.

According to the models of Saio et al. (2013), the radial modes, especially in late-type stars, display the longest periods. Therefore, for each star we searched for correlations with the longest known period. As shown in Fig. 11, we found a linear correlation for stars mostly represented by mid/late BSGs (i.e. spectral type from B2 to B9) with $P > 6$ days. The longer the period the lower the amplitude of the parameter Q_r . We added to our sample two well-studied variable stars having measurements of their stellar and wind parameters (Deneb and 55 Cyg, Scuderi et al. 1992; Chesneau et al. 2010; Kraus et al. 2015). Three mid-type BSGs with measured values of P and \dot{M} were rejected from the sample: HD 53138, HD 75149, and HD 99953 (Fig. 11, green dots without triangles). Two of these stars HD 75149 and HD 99953 have been poorly studied and new periods should probably be determined. The former, in particular, might have inaccurate minimum values of \dot{M} since two of our observed profiles are in absorption. The star HD 111973 is not included since we have observations during an interval of time of two days which is less than the reported period of variation.

The relationship we obtained is $P_{\text{max}} = 100.27(\pm 7.64) X + 83.97(\pm 4.47)$, where $X = \log Q_{r\text{min}} / Q_{r\text{max}}$, and was derived using the data enclosed in triangles (the used values of $Q_{r\text{min}}$ and $Q_{r\text{max}}$ are listed in bold in Table A.1). The differences in the selected values are two or three times larger than their corresponding error bars, suggesting real variations in the mass-loss rates.

The group that comprises the early BSGs (HD 38771, the binary star HD 47420, HD 52089, HD 64760, and HD 148688, blue diamonds) does not show a clear correlation with their periods. Some of these stars show differences in their Q_r parameters of the order of the errors suggesting that they do not show strong wind variability.

We can then conclude that as the observed line profiles can be matched using a velocity β -law, radiation pressure is the main mechanism that drives the wind. However, pulsation modes may also play a significant role in (quasi-)periodically lifting the material, which will then be accelerated outwards by radiation. In this way, radial strange-mode pulsation with periods > 6 days

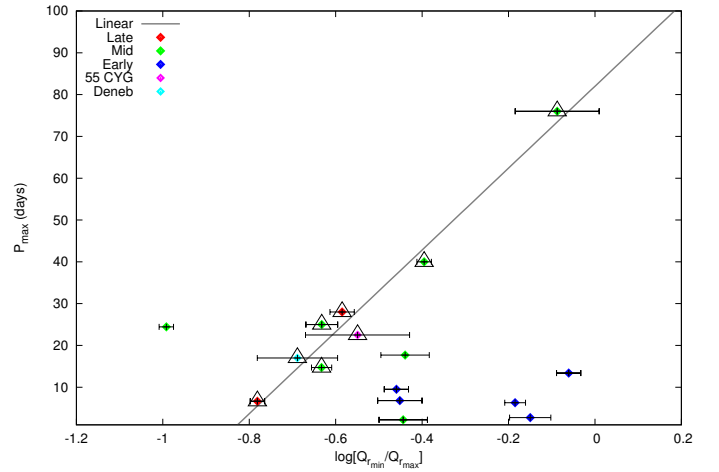


Fig. 11. Ratios between minimum and maximum Q_r values as a function of the longest photometric/spectroscopic period, where $Q_r = \dot{M}/R^{1.5}$. The linear correlation was obtained using the up-pointing triangle.

might be responsible for the wind variability in mid- and late-type BSGs.

5.5. Location of the BSGs in the HR diagram.

Figure 12 displays the position of our sample stars in the HR diagram, using data from Table 3, together with the stability boundaries for the different pulsation modes, as defined by Saio et al. (2013). The stability boundary for low-order radial and non-radial p modes is represented by the blue solid line. This bends and becomes horizontal due to strange-mode instability which occurs when $\log L/M > 4$. Non-radial modes (low-degree high-order g -modes) can be excited in the region delimited by red lines, whilst monotonically unstable modes exist above the magenta dotted line in the most luminous part of the HR diagram (as is the case for the hypergiant star HD 80077). On the other hand, two stars in our sample (HD 52089 and HD 64760, with $\log L/L_\odot < 4.6$, $\log L/M < 4$) are located inside the instability strip of the β Cep, found by Saio et al. (2013) and Georgy et al. (2014), near the cool border of that region. Particularly, HD 64740 presents in the UV spectral region clear signs of phase bowing and ionization changes in the wind that could be associated with strong shocks originating in the interface between slow and fast wind streams, such as in a model of co-rotating interaction regions (Prinja et al. 2002), and its WISE image reveals a

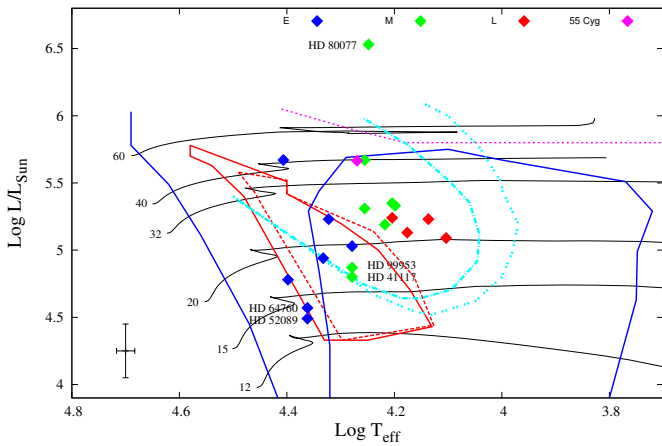


Fig. 12. Position of the sample of stars in the HR diagram. Evolutionary tracks (taken from Ekström et al. 2012, black solid lines) correspond to non-rotating stars with $M_* = 12, 15, 20, 32, 40$, and $60 M_\odot$. The coloured curves define instability boundaries of various modes (Saio 2011): a) stability boundary for low-order radial and non-radial p modes (blue solid line); b) non-radial g modes with $l=1$ and 2 (red short-dashed and solid lines, respectively); c) oscillatory convection modes (cyan dot-dashed lines); d) monotonically unstable radial modes (above the magenta dotted-line, where the hypergiant star HD 80077 is found). The blue, green, red, and magenta diamonds correspond to early (E), mid (M), and late (L) BSGs, and 55 Cyg, respectively.

kind of wind-lobe structure. We propose that this star could be evolving towards the RSG stage.

In the same HR diagram we can also see that the mid-/late-type stars are located in the region where oscillatory convection modes would be observable (cyan lines, Saio 2011; Saio et al. 2013), with the exception of HD 4117 and HD 9953, which are located together with the early B types. The star 55 Cyg (taken from Kraus et al. 2015) was also included.

It is worth mentioning that WISE images reveal signs of previous strong wind-ISM interaction in three objects in our sample (HD 52382, HD 9953, and HD 115842) pointing out that these stars could be evolving towards the blue-loop after a post-RSG phase. This same also holds true for 55 Cyg (Kraus et al. 2015).

6. Conclusions

We studied a sample of 19 Galactic BSGs by fitting theoretical line profiles of H, He, and Si to the observed profiles. The synthetic line profiles were computed with the NLTE atmosphere code FASTWIND to obtain new estimates for their stellar and wind parameters. The mass-loss rates for HD 74371, HD 9953, and HD 111973 have been derived for the first time. In addition, some BSGs in our sample show short-term variability in the $H\alpha$ and UV resonance lines, indicating important changes in the wind structure.

In relation with the global properties of the stellar winds of our sample, we find two different behaviours in the WLR. The early and mid B-type stars have mostly $\beta < 2$ and terminal velocities greater than 500 km s^{-1} , while the other group is comprised mostly by mid and late B-type stars with $\beta \geq 2$ and terminal velocities lower than 500 km s^{-1} . In addition, we find that the coefficients for the linear regression of early BSGs agree with theoretical or empirical values found by Vink (2000); Herrero et al. (2002); Mokiem et al. (2007). As well, our coefficients would

agree with data from Searle et al. (2008) if we separated their sample of stars into two groups: early and mid BSGs.

Furthermore, we observe that a decrease in the ratio V_∞/V_{esc} in the bi-stability region, and on its cool side, is accompanied by a decrease in mass-loss rate. This observation is contrary to the theoretical result obtained by Vink et al. (1999), based on a fast wind regime. Instead, this behaviour seems to be consistent with predictions from highly ionized stellar winds (δ – *slow* solution, Venero et al. 2016). The possible switch between fast and δ – *slow* solutions should be explored in detail.

Finally, we found an empirical correlation (period–mass-loss relationship) that associates the amplitude of the mass-loss variations with long-term photometric and/or spectroscopic variability. This relation is expressed in terms of the Q_r parameter. The found period–mass-loss relationship could indicate that radial (or strange) pulsation modes with periods > 6 days are related to the wind variability. To confirm this trend, it is necessary to perform long-term high-resolution spectroscopic campaigns to properly measure oscillation periods and simultaneously derive homogeneous sets of mass-loss rates.

Acknowledgements. We thank our anonymous referee for the helpful comments and suggestions. We also want to acknowledge J. Puls for allowing us to use the FASTWIND code, for his help and advice with the code, and for the fruitful suggestions. This research has also made use of the SIMBAD database, operated at CDS, Strasbourg, France, and the International Variable Star Index (VSX) database, operated at AAVSO, Cambridge, Massachusetts, USA. L.C. and M.C. acknowledge support from the project CONICYT + PAI/Atracción de capital humano avanzado del extranjero (folio PA180160057). L.C. also acknowledges financial support from CONICET (PIP 0177), La Agencia Nacional de Promoción Científica y Tecnológica (PICT 2016–1971) and the Programa de Incentivos (G11/137) of the Universidad Nacional de La Plata (UNLP), Argentina. R.V. is grateful for the financial support from the UNLP under programme PPID/G003. M.C., S.K., and C.A. acknowledge support from Centro de Astrofísica de Valparaíso. C.A. also thanks BECAS DE DOCTORADO NACIONAL CONICYT 2016–2017. M.K. acknowledges support from GAČR (17-02337S). The Astronomical Institute Ondřejov is supported by the project RVO:67985815. This work was partly supported by the European Union European Regional Development Fund, project “Benefits for Estonian Society from Space Research and Application” (KOMEET, 2014–2020.4.01.16–0029), and by the institutional research funding IUT40–1 of the Estonian Ministry of Education and Research. Financial support for International Cooperation of the Czech Republic and Argentina (AVCR-CONICET/14/003) is acknowledged.

References

- Abbott, D. C. 1982, *ApJ*, 259, 282
- Aerts, C., Lefever, K., Baglin, A., et al. 2010, *A&A*, 513, L11
- Aerts, C., Simón-Díaz, S., Catala, C., et al. 2013, *A&A*, 557, A114
- Astraatmadja, T. L. & Bailer-Jones, C. A. L. 2016, *ApJ*, 833, 119
- Barlow, M. J. & Cohen, M. 1977, *ApJ*, 213, 737
- Benaglia, P., Vink, J. S., Martí, J., et al. 2007, *A&A*, 467, 1265
- Bouret, J.-C., Lanz, T., & Hillier, D. J. 2005, *A&A*, 438, 301
- Carpay, J., de Jager, C., & Nieuwenhuijzen, H. 1991, *A&A*, 248, 475
- Carpay, J., de Jager, C., Nieuwenhuijzen, H., & Moffat, A. 1989, *A&A*, 216, 143
- Castor, J. I., Abbott, D. C., & Klein, R. I. 1975, *ApJ*, 195, 157
- Chesneau, O., Dessart, L., Mourard, D., et al. 2010, *A&A*, 521, A5
- Chesneau, O., Kaufer, A., Stahl, O., et al. 2014, *A&A*, 566, A125
- Chini, R., Hoffmeister, V. H., Nasserri, A., Stahl, O., & Zinnecker, H. 2012, *MNRAS*, 424, 1925
- Cidale, L. S. & Ringuelet, A. E. 1993, *ApJ*, 411, 874
- Cohen, D. H., Cooper, R. G., Macfarlane, J. J., et al. 1996, *ApJ*, 460, 506
- Crowther, P. A., Lennon, D. J., & Walborn, N. R. 2006, *A&A*, 446, 279
- Curé, M., Cidale, L., & Granada, A. 2011, *ApJ*, 737, 18
- Ebbets, D. 1982, *ApJS*, 48, 399
- Ekström, S., Georgy, C., Eggenberger, P., et al. 2012, *A&A*, 537, A146
- Evans, C. J., Lennon, D. J., Trundle, C., Heap, S. R., & Lindler, D. J. 2004, *ApJ*, 607, 451
- Feldmeier, A. 1998, *A&A*, 332, 245
- Firnstein, M. & Przybilla, N. 2012, *A&A*, 543, A80
- Flower, P. J. 1996, *ApJ*, 469, 355
- Fraser, M., Dufton, P. L., Hunter, I., & Ryans, R. S. I. 2010, *MNRAS*, 404, 1306
- Frémat, Y., Zorec, J., Hubert, A., & Floquet, M. 2005, *A&A*, 440, 305

- Friend, D. B. & Abbott, D. C. 1986, *ApJ*, 311, 701
- Fullerton, A. W., Massa, D. L., & Prinja, R. K. 2006, *ApJ*, 637, 1025
- Garcia, M., Herrero, A., Najarro, F., et al. 2017, *ArXiv e-prints* [arXiv:1703.00218]
- Garmany, C. D., Olson, G. L., van Steenberg, M. E., & Conti, P. S. 1981, *ApJ*, 250, 660
- Gathier, R., Lamers, H. J. G. L. M., & Snow, T. P. 1981, *ApJ*, 247, 173
- Georgy, C., Saio, H., & Meynet, G. 2014, *MNRAS*, 439, L6
- Glatzel, W., Kiriakidis, M., Chernigovskij, S., & Fricke, K. J. 1999, *MNRAS*, 303, 116
- Godart, M., Simón-Díaz, S., Herrero, A., et al. 2017, *A&A*, 597, A23
- Grevesse, N. & Sauval, A. J. 1998, *Space Sci. Rev.*, 85, 161
- Henrichs, H. F., Neiner, C., & Geers, V. C. 2003, in *IAU Symposium*, Vol. 212, *A Massive Star Odyssey: From Main Sequence to Supernova*, ed. K. van der Hucht, A. Herrero, & C. Esteban, 202
- Herrero, A., Puls, J., & Najarro, F. 2002, *A&A*, 396, 949
- Hillier, D. J. & Miller, D. L. 1998, *ApJ*, 496, 407
- Hoffleit, D. & Jaschek, C. 1991, *The Bright Star Catalogue*, New Haven, Conn.: Yale University Observatory, c1991, 5th rev.ed., edited by Hoffleit, Dorrit; Jaschek, Carlos
- Howarth, I. D., Siebert, K. W., Hussain, G. A. J., & Prinja, R. K. 1997, *MNRAS*, 284, 265
- Hubeny, I. & Lanz, T. 1995, *ApJ*, 439, 875
- Humphreys, R. M. 1978, *ApJS*, 38, 309
- Israelian, G., Chentsov, E., & Musaev, F. 1997, *MNRAS*, 290, 521
- Jaschek, M. & Brandi, E. 1973, *PASP*, 85, 736
- Kaufer, A., Stahl, O., Prinja, R. K., & Witherick, D. 2006, *A&A*, 447, 325
- Knoechel, G. & Moffat, A. F. J. 1982, *A&A*, 110, 263
- Koen, C. & Eyer, L. 2002, *MNRAS*, 331, 45
- Kraus, M., Haucke, M., Cidale, L. S., et al. 2015, *A&A*, 581, A75
- Kraus, M., Tomić, S., Oksala, M. E., & Smole, M. 2012, *A&A*, 542, L32
- Krtićka, J. & Kubát, J. 2001, *A&A*, 377, 175
- Kudritzki, R.-P., Lennon, D. J., & Puls, J. 1995, in *Science with the VLT*, ed. J. R. Walsh & I. J. Danziger, 246
- Kudritzki, R. P., Puls, J., Lennon, D. J., et al. 1999, *A&A*, 350, 970
- Kurucz, R. L. 1979, *ApJS*, 40, 1
- Lamers, H. J. G. L. M., Gathier, R., & Snow, Jr., T. P. 1982, *ApJ*, 258, 186
- Lamers, H. J. G. L. M., Snow, T. P., & Lindholm, D. M. 1995, *ApJ*, 455, 269
- Lanz, T. & Hubeny, I. 2007, *ApJS*, 169, 83
- Lefever, K., Puls, J., & Aerts, C. 2007, *A&A*, 463, 1093
- Lefever, K., Puls, J., Morel, T., et al. 2010, *A&A*, 515, A74
- Lefèvre, L., Marchenko, S. V., Moffat, A. F. J., & Acker, A. 2009, *A&A*, 507, 1141
- Marco, A. & Negueruela, I. 2009, *A&A*, 493, 79
- Markova, N., Prinja, R. K., Markov, H., et al. 2008, *A&A*, 487, 211
- Markova, N. & Puls, J. 2008, *A&A*, 478, 823
- Markova, N., Puls, J., Repolust, T., & Markov, H. 2004, *A&A*, 413, 693
- Massa, D., Fullerton, A. W., Nichols, J. S., et al. 1995, *ApJ*, 452, L53
- McErlean, N. D., Lennon, D. J., & Dufton, P. L. 1999, *A&A*, 349, 553
- Megier, A., Strobel, A., Galazutdinov, G. A., & Krelowski, J. 2009, *A&A*, 507, 833
- Meynet, G., Maeder, A., Schaller, G., Schaerer, D., & Charbonnel, C. 1994, *A&AS*, 103, 97
- Mokiem, M. R., de Koter, A., Vink, J. S., et al. 2007, *A&A*, 473, 603
- Moravveji, E., Guinan, E. F., Shultz, M., Williamson, M. H., & Moya, A. 2012, *ApJ*, 747, 108
- Morel, T., Hubrig, S., & Briquet, M. 2008, *A&A*, 481, 453
- Morel, T., Marchenko, S. V., Pati, A. K., et al. 2004, *MNRAS*, 351, 552
- Nerney, S. 1980, *ApJ*, 242, 723
- Oskinova, L. M., Hamann, W.-R., & Feldmeier, A. 2007, *A&A*, 476, 1331
- Owocki, S. P., Castor, J. I., & Rybicki, G. B. 1988, *ApJ*, 335, 914
- Owocki, S. P. & Rybicki, G. B. 1984, *ApJ*, 284, 337
- Pasinetti Fracassini, L. E., Pastori, L., Covino, S., & Pozzi, A. 2001, *A&A*, 367, 521
- Pauldrach, A., Puls, J., & Kudritzki, R. P. 1986, *A&A*, 164, 86
- Pauldrach, A. W. A. & Puls, J. 1990, *A&A*, 237, 409
- Peri, C. S., Benaglia, P., Brookes, D. P., Stevens, I. R., & Isequilla, N. L. 2012, *A&A*, 538, A108
- Petrov, B., Vink, J. S., & Gräfener, G. 2014, *A&A*, 565, A62
- Prinja, R. K., Barlow, M. J., & Howarth, I. D. 1990, *ApJ*, 361, 607
- Prinja, R. K. & Howarth, I. D. 1986, *ApJS*, 61, 357
- Prinja, R. K., Massa, D., & Fullerton, A. W. 1995, *ApJ*, 452, L61
- Prinja, R. K., Massa, D., & Fullerton, A. W. 2002, *A&A*, 388, 587
- Prinja, R. K., Massa, D., Howarth, I. D., & Fullerton, A. W. 1998, *MNRAS*, 301, 926
- Prinja, R. K. & Massa, D. L. 2010, *A&A*, 521, L55
- Prinja, R. K. & Massa, D. L. 2013, *A&A*, 559, A15
- Prinja, R. K., Rivinius, T., Stahl, O., et al. 2004, *A&A*, 418, 727
- Prugniel, P., Vauglin, I., & Koleva, M. 2011, *A&A*, 531, A165
- Przybilla, N., Butler, K., Becker, S. R., & Kudritzki, R. P. 2006, *A&A*, 445, 1099
- Puls, J. 1991, *A&A*, 248, 581
- Puls, J., Kudritzki, R.-P., Herrero, A., et al. 1996, *A&A*, 305, 171
- Puls, J., Urbaneja, M. A., Venero, R., et al. 2005, *A&A*, 435, 669
- Puls, J., Vink, J. S., & Najarro, F. 2008, *A&A Rev.*, 16, 209
- Rivero González, J. G., Puls, J., Najarro, F., & Brott, I. 2012, *A&A*, 537, A79
- Rusconi, L., Sedmak, G., Stalio, R., & Arpigny, C. 1980, *A&AS*, 42, 347
- Saio, H. 2011, *MNRAS*, 412, 1814
- Saio, H., Georgy, C., & Meynet, G. 2013, *MNRAS*, 433, 1246
- Saio, H., Kuschnig, R., Gautschi, A., et al. 2006, *ApJ*, 650, 1111
- Santolaya-Rey, A. E., Puls, J., & Herrero, A. 1997, *A&A*, 323, 488
- Scuderi, S., Bonanno, G., di Benedetto, R., Spadaro, D., & Panagia, N. 1992, *ApJ*, 392, 201
- Scuderi, S., Panagia, N., Stanghellini, C., Triglio, C., & Umana, G. 1998, *A&A*, 332, 251
- Searle, S. C., Prinja, R. K., Massa, D., & Ryans, R. 2008, *A&A*, 481, 777
- Simón-Díaz, S. & Herrero, A. 2007, *A&A*, 468, 1063
- Simón-Díaz, S. & Herrero, A. 2014, *A&A*, 562, A135
- Sterken, C. 1977, *A&A*, 57, 361
- Sundqvist, J. O., Puls, J., & Feldmeier, A. 2010, *A&A*, 510, A11
- Sundqvist, J. O., Puls, J., Feldmeier, A., & Owocki, S. P. 2011, *A&A*, 528, A64
- Tomić, S., Kraus, M., & Oksala, M. E. 2015, in *IAU Symposium*, Vol. 307, *New Windows on Massive Stars*, ed. G. Meynet, C. Georgy, J. Groh, & P. Stee, 235–236
- Underhill, A. B. 1984, *ApJ*, 285, 668
- Šurlan, B., Hamann, W.-R., Aret, A., et al. 2013, *A&A*, 559, A130
- van Breda, I. G., Glass, I. S., & Whittet, D. C. B. 1974, *MNRAS*, 168, 551
- van Genderen, A. M., Bovenschen, H., Engelsman, E. C., et al. 1989, *A&AS*, 79, 263
- van Leeuwen, F. 2007, *A&A*, 474, 653
- van Leeuwen, F., van Genderen, A. M., & Zegelaar, I. 1998, *A&AS*, 128, 117
- Venero, R. O. J., Cidale, L. S., Cure, M., & Haucke, M. 2017, *Boletín de la Asociacion Argentina de Astronomia La Plata Argentina*, 59, 28
- Venero, R. O. J., Curé, M., Cidale, L. S., & Araya, I. 2016, *ApJ*, 822, 28
- Vink, J. S. 2000, PhD thesis, Universiteit Utrecht
- Vink, J. S., de Koter, A., & Lamers, H. J. G. L. M. 1999, *A&A*, 350, 181
- Vink, J. S., de Koter, A., & Lamers, H. J. G. L. M. 2001, *A&A*, 369, 574
- Wenger, M., Ochsenbein, F., Egret, D., et al. 2000, *A&AS*, 143, 9
- Woosley, S. E., Heger, A., & Weaver, T. A. 2002, *Reviews of Modern Physics*, 74, 1015
- Wright, E. L., Eisenhardt, P. R. M., Mainzer, A. K., et al. 2010, *AJ*, 140, 1868
- Yadav, A. P. & Glatzel, W. 2016, *MNRAS*, 457, 4330
- Zorec, J., Cidale, L., Arias, M. L., et al. 2009, *A&A*, 501, 297
- Zorec, J., Frémat, Y., & Cidale, L. 2005, *A&A*, 441, 235

Appendix A: Photospheric line-fitting and compiled data from the literature

The following figures present a comparison between observed and synthetic photospheric line profiles calculated with FAST-WIND and the parameters quoted in Table 3. These parameters are also given in Table A.1 together with a set of stellar and wind parameters gathered from the literature.

Table A.1. Stellar and wind parameters.

Name	T_{eff} K	$\log g_{\text{eff}}$ dex	$\log g_{\text{cor}}$ dex	β	\dot{M} $10^{-6} M_{\odot} \text{ yr}^{-1}$	V_{∞} km s^{-1}	V_{micro} km s^{-1}	V_{macro} km s^{-1}	$V \sin i$ km s^{-1}	R_{\star} R_{\odot}	$\log(L/L_{\odot})$ dex	$\log Q$	$\log Q_r$	References
HD 34085	12 700 12 000 12 100 12 500 12 000 13 000 13 000 ...	1.70 ... 1.75 1.70 1.75 1.75 1.75 1.60	1.72	2.6	0.23 0.76/0.94 ... 0.34 0.86/1.4	155 300 ... 230/350 400/600	10 8	52 35 22 40 40	30 36 25 30 36 ... 33	72 115 ... 129 109 ... 135	5.09 5.45 ... 5.56 5.34 4.87 ...	-12.71 -12.93/-12.83 ... -13.35/-13.08 -13.35/-13.14	-9.42 ± 0.17 -9.21/-9.12 ... -9.63 ± 0.17 -9.26/-9.05	This work Chesneau et al. (2014) Firnstein & Przybilla (2012) Markova et al. (2008) Przybilla et al. (2006) McErlean et al. (1999) Israelian et al. (1997) Nerney (1980)
HD 38771	25 000 26 000 26 500 27 500 27 500 26 000 ...	2.70 3.00 2.70 3.00 3.00 3.07 ...	2.76 ... 2.90 2.94 ...	1.5 1.1 1.5 1.0	0.14 1.20 0.90 0.27 ... 0.7/1.1	1 500 1 390 1 525 1 350 ... 1 870 1 900/3 450	13 15 12.5 10	60	80 91 83 80 81 82	13 27.0 22.2 13.0 ... 28 30	4.78 5.48 5.35 4.94 4.68 5.52 ...	-13.29 -12.78 -12.84 -12.94 ... -13.68/-13.09 -12.78	-8.52 ± 0.20 -8.07 ± 0.17 -8.07 -8.24 ± 0.13 ... -8.37/-8.10 -8.81 ± 0.14	This work Searle et al. (2008) Crowther et al. (2006) Kudritzki et al. (1999) McErlean et al. (1999) Gathier et al. (1981) Nerney (1980)
HD 41117	19 000 20 000 19 000 19 500 19 500 18 500 ...	2.30 2.40 2.10 2.25 2.20	2.32 ... 2.35	2.0 ... 2.0 1.0	0.17 ... 0.90 0.85 1.6 2.2	510 ... 510 500 ... 510 1 000	10 ... 10 20	65 65	40 ... 72 40 ... 36	23 61.9 61.7 ... 58 63.4	4.84 ... 5.65 5.70 5.55	-12.78 ... -12.79 -12.8 -12.5 -12.86 -8.73 -8.76 ± 0.13 ... -8.44 -8.36	This work Prugniel et al. (2011) Crowther et al. (2006) Kudritzki et al. (1999) McErlean et al. (1999) Scuderi et al. (1998) Nerney (1980)
HD 42087	16 500 18 000 19 000 17 150 20 500 20 500 ...	2.45 2.50 2.30 ... 2.50 2.55 ...	2.47	2.0 1.2 3.0 ...	0.57 0.50 0.20 0.20 0.11 0.24	700 650 ... 735 735 450	15 15 40 10	80 60	80 71 ... 71 60 95	55 36.6 ... 26.0 35.2 30	5.31 5.11 5.08 ... 5.30 4.96	-13.12 -12.87 ... -13.12 -13.58 ...	-8.85 ± 0.11 -8.65 ± 0.33 ... -8.82 -9.28 ± 0.13 ... -8.84 ± 0.11	This work Searle et al. (2008) Benaglia et al. (2007) Morel et al. (2004) Kudritzki et al. (1999) McErlean et al. (1999)
HD 47240	19 000 19 000 23 000 20 100 22 000 22 200 ...	2.40 2.40 3.00 3.05 3.20 3.22 ...	2.47 2.48 3.00	1.0 1.5 1.0	0.24 0.17 - 0.24 0.02	450 1 000 900	10 15 8 17 15 16	60 55 65 17 20 ...	95 94 10 22 32 ...	30 27 11	5.03 4.93 4.49	-12.82 -13.42/-13.27 -13.69	-8.84 ± 0.11 -8.92 ± 0.25 / -8.77 ± 0.25 -9.26 ± 0.2	This work Lefever et al. (2007)
HD 52089	23 000 20 100 22 000 22 200 21 500 23 000 20 800 ...	3.00 3.05 3.20 3.22 2.45	3.00 2.48 2.71 ...	1.0 2.2	0.02 0.24 ... 0.49	900 1 000 1 200 ...	8 20 ...	65 53 ...	10 22 32 ... 55 56 ...	11 21 ...	4.49 4.94 ...	-13.69 -13.10 -8.60 ± 0.13	This work Fraser et al. (2010) Lefever et al. (2010) Morel et al. (2008)
HD 53138	18 000 15 400 16 500 17 000 15 500 18 500 ...	2.25 2.15 2.25 2.15 1.75 2.30 2.35 ...	2.26 2.16 2.05	2.0 ... 1.2 2.5 2.0	0.2/0.24 ... 0.45 0.21/0.31 0.36 0.095 1.7	600/450 ... 500 490 865 620 580	10 18 20 15 20	60 23 ... 45 38 40 ...	40 35 58 58 65 55 59.1	46 ... 54.7 50 65 39.6 ...	5.31 ... 5.30 5.27 5.34 5.22 5.04	-13.36/-13.09 ... -13.00 -13.20 -13.57	-9.19 ± 0.11 / -9.11 ± 0.11 ... -8.95 ± 0.17 -9.23 ± 0.25 / -9.06 ± 0.25 -9.16 -9.42 ± 0.13 ... -8.43	This work Fraser et al. (2010) Searle et al. (2008) Lefever et al. (2007) Crowther et al. (2006) Kudritzki et al. (1999) McErlean et al. (1999) Nerney (1980)
HD 58350	15 000 – 16 000 14 500 15 000 13 500 16 000 23 000 26 000 28 000 ...	2.00 2.10 2.13 1.75 2.10 ... 3.25 3.38 ...	2.02 1.77 3.09	3.0 ... 1.0 2.5 0.5 1.0	0.116-0.15 ... 0.70 0.14 ... 0.42 ... 1.10	175-233 ... 320 250 ... 1 500 1 600 ...	11 18 20 12 ... 22 15	50/70 25 ... 40	40 32 50 37 ... 255 265	54 ... 57.3 65 ... 12 23.3	5.13-5.24 ... 5.18 5.10 5.36 4.57 5.48	-12.9/-12.97 ... -12.55 -13.17 ... -12.76 -12.82	-9.53 ± 0.13 / -9.42 ± 0.13 ... -8.79 ± 0.23 -9.57 ± 0.25 ... -8.00 ± 0.13 -8.01 ± 0.17	This work Fraser et al. (2010) Searle et al. (2008) Lefever et al. (2007) McErlean et al. (1999) This work Fraser et al. (2010) Searle et al. (2008)

Table A.1. Continued.

Name	T_{eff} K	$\log g_{\text{eff}}$ dex	$\log g_{\text{cor}}$ dex	β	M $10^{-6} M_{\odot} \text{yr}^{-1}$	V_{∞} km s^{-1}	V_{micro} km s^{-1}	V_{macro} km s^{-1}	$V \sin i$ km s^{-1}	R_{\star} R_{\odot}	$\log L/L_{\odot}$ dex	$\log Q$	$\log Q_r$	References
HD 74371	24 000	3.20	3.27	0.8	0.42	1 400	14	...	230	24	5.23	-13.16	-8.45±0.25	Lefever et al. (2007)
	13 700	1.80	1.81	2	0.28	200	10	60	30	73	5.23	-12.8	-9.35 ± 0.11	This work
	13 400	1.90	20	30	31	Fraser et al. (2010)
HD 75149	16 000	2.10	2.11	2.5	0.09/0.25	400/350	9/17	55/60	40	61	5.35	-13.63/-13.1	-9.72±0.15/-9.28±0.15	This work
	15 900	2.20	20	34	30	Fraser et al. (2010)
	16 000	2.05	2.06	2.5	0.10	500	15	60	30	39	4.95	-13.43	-9.39 ± 0.25	Lefever et al. (2007)
HD 79186	15 800	2.0	2.02	3.3	0.40	400	11	53	40	61	5.33	-12.98	-9.08 ± 0.09	This work
	15 100	2.0	14	36	39	Fraser et al. (2010)
	15 000	0.80	435	Prinja & Massa (2010)
	13 600	0.66	450	62.4	...	-12.85	-8.87 ± 0.09	Krtićka & Kubát (2001)
	13 900	45	81	Underhill (1984)
HD 80077	17 700	2.20	2.20	3-3.2	5.4	150/200	10	60	10	195	6.53	-11.97/12.15	-8.70±0.11	This work
	17 000	2.00	5.00	140	162	6.3	-11.83	-8.62±0.65	Carpay et al. (1989)
	18 500	2.25	1.70	140	5.4	Benaglia et al. (2007)
HD 92964	18 000	2.20	2.21	2.0	0.49	370	11	40	45	70	5.67	-12.93	-9.08 ± 0.09	This work
	15 600	2.00	22	28	36	Fraser et al. (2010)
	18 000	2.10	2.10	3.0	0.25/0.28	520	15	50	31	48	5.33	-13.14/-13.19	-9.07±0.25	Lefever et al. (2007)
	17 400	0.11	530/807	68	...	-13.79/-14.07	-9.71	Krtićka & Kubát (2001)
HD 99953	19 000	2.30	2.33	2.0	0.08/0.22	250/700	18	50	50	25	4.87	-12.79/-13.02	-9.19±0.11/-8.75±0.11	This work
	16 800	2.15	22	37	49	Fraser et al. (2010)
HD 111973	16 500	2.10	2.11	2.0	0.14/0.21	350	12	~60	35	48	5.16	-13.19/-13.02	-9.38 ± 0.09 / -9.20 ± 0.09	This work
	16 000	2.30	19	28	36	Fraser et al. (2010)
	16 500	0.5	...	520	Prinja & Massa (2010)
HD 115842	25 500	2.75	2.76	2.5	1.8	1 700	10	120	70	35	5.68	-12.91	-8.06±0.13	This work
	24 800	2.75	14	66	39	Fraser et al. (2010)
	25 500	2.65	2.85	1.5	2.0	1 180	10	...	84	34.2	5.65	-12.61	-8.00	Crowther et al. (2006)
HD 148688	21 000	2.45	2.47	2.5	1.15	1 200	11	65	50	31	5.23	-12.8	-8.18 ± 0.15	This work
	20 700	2.45	16	44	48	Fraser et al. (2010)
	21 000	2.50	2.5	3.0	1.10/1.40	1 200	15	40	50	42	5.49	-12.90/-13.01	-8.29 ± 0.25	Lefever et al. (2007)
	22 000	2.40	2.60	2.0	1.75	725	15	...	72	36.7	5.45	-12.39	-8.10	Crowther et al. (2006)

Highlighted values were used to make Fig. 11.

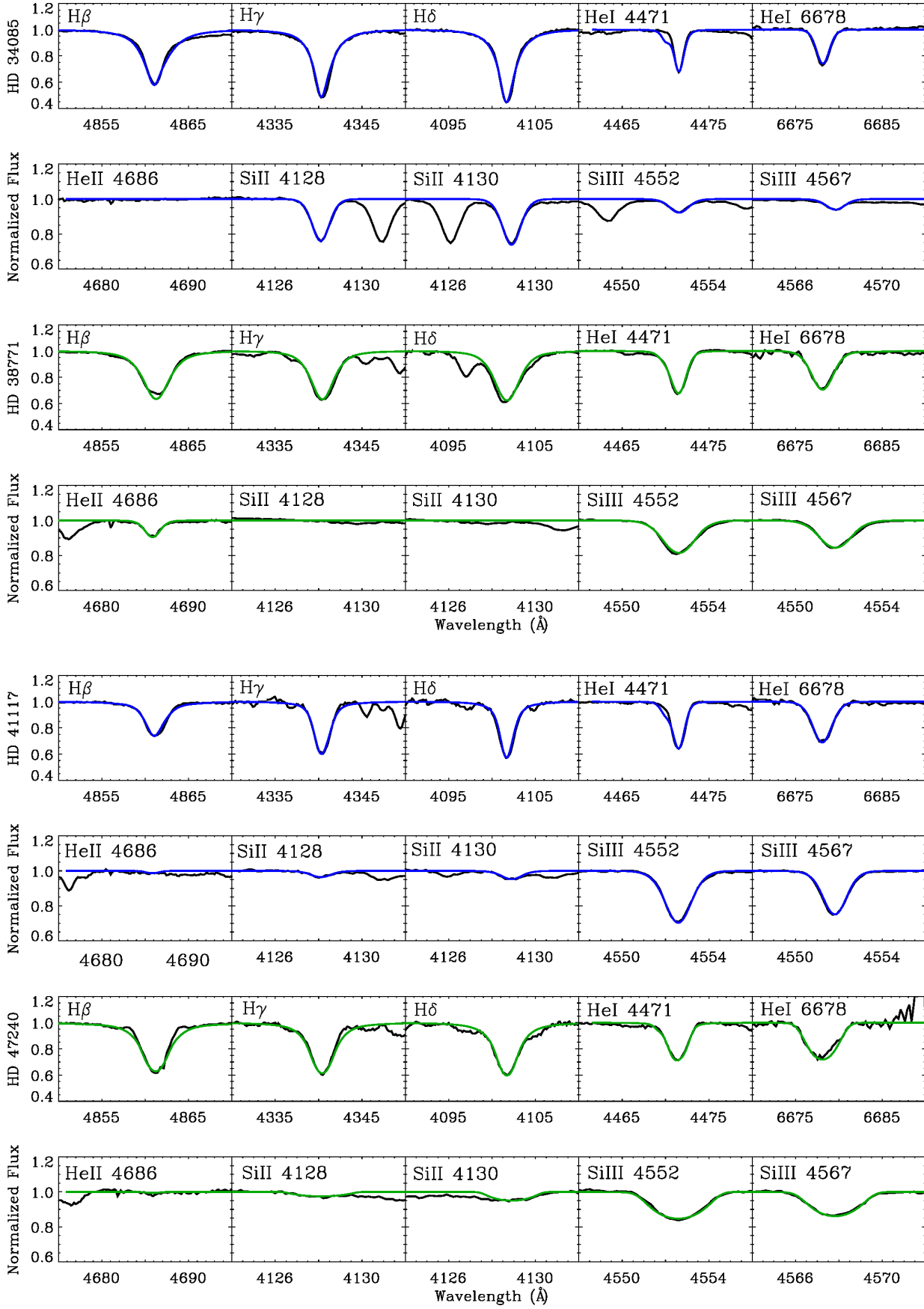


Fig. A.1. HD 34085, HD 38771, HD 41117, and HD 47240: Line model fittings to observations.

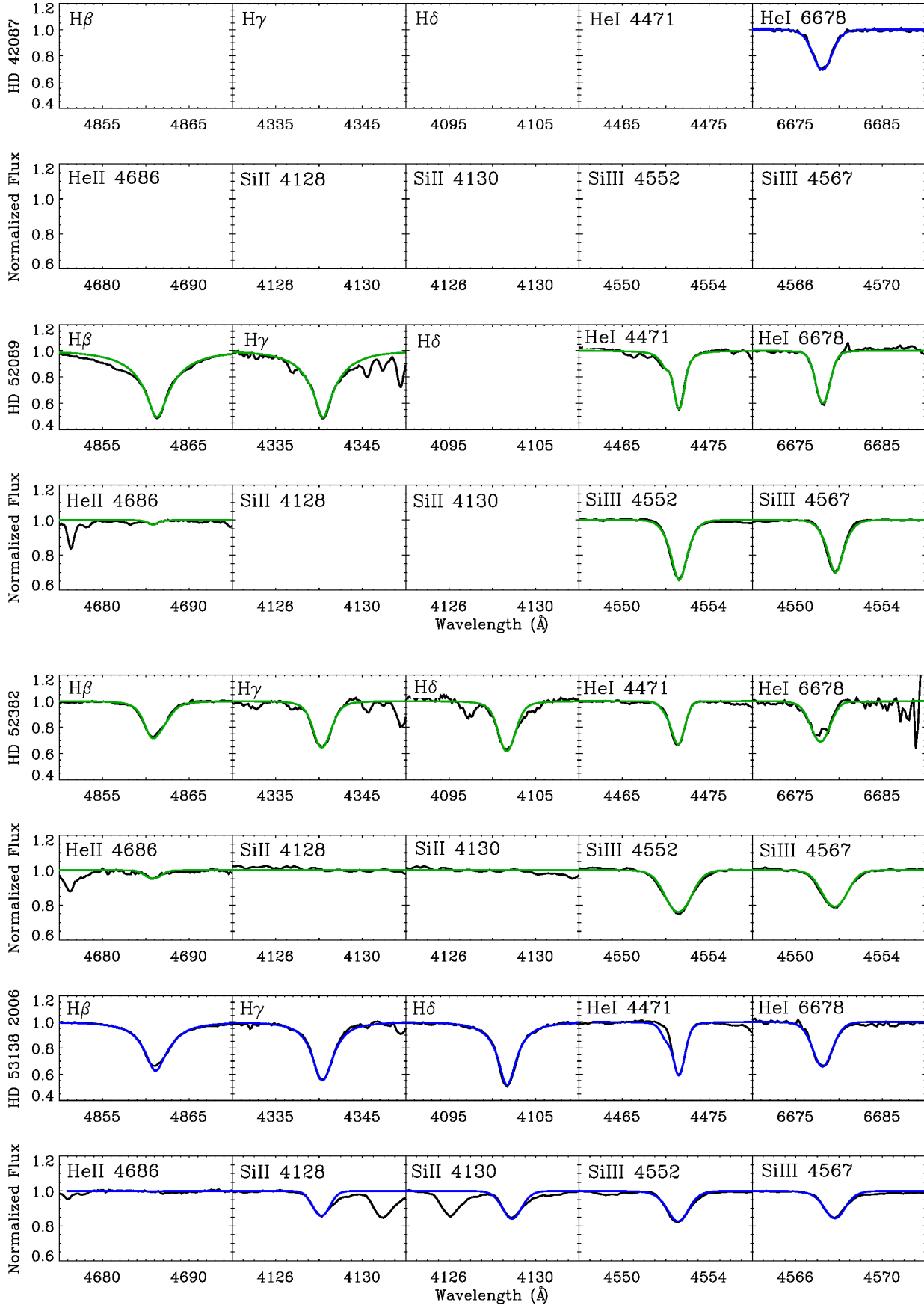


Fig. A.2. HD 42087, HD 52089, HD 52382, and HD 53138: Line model fittings to observations.

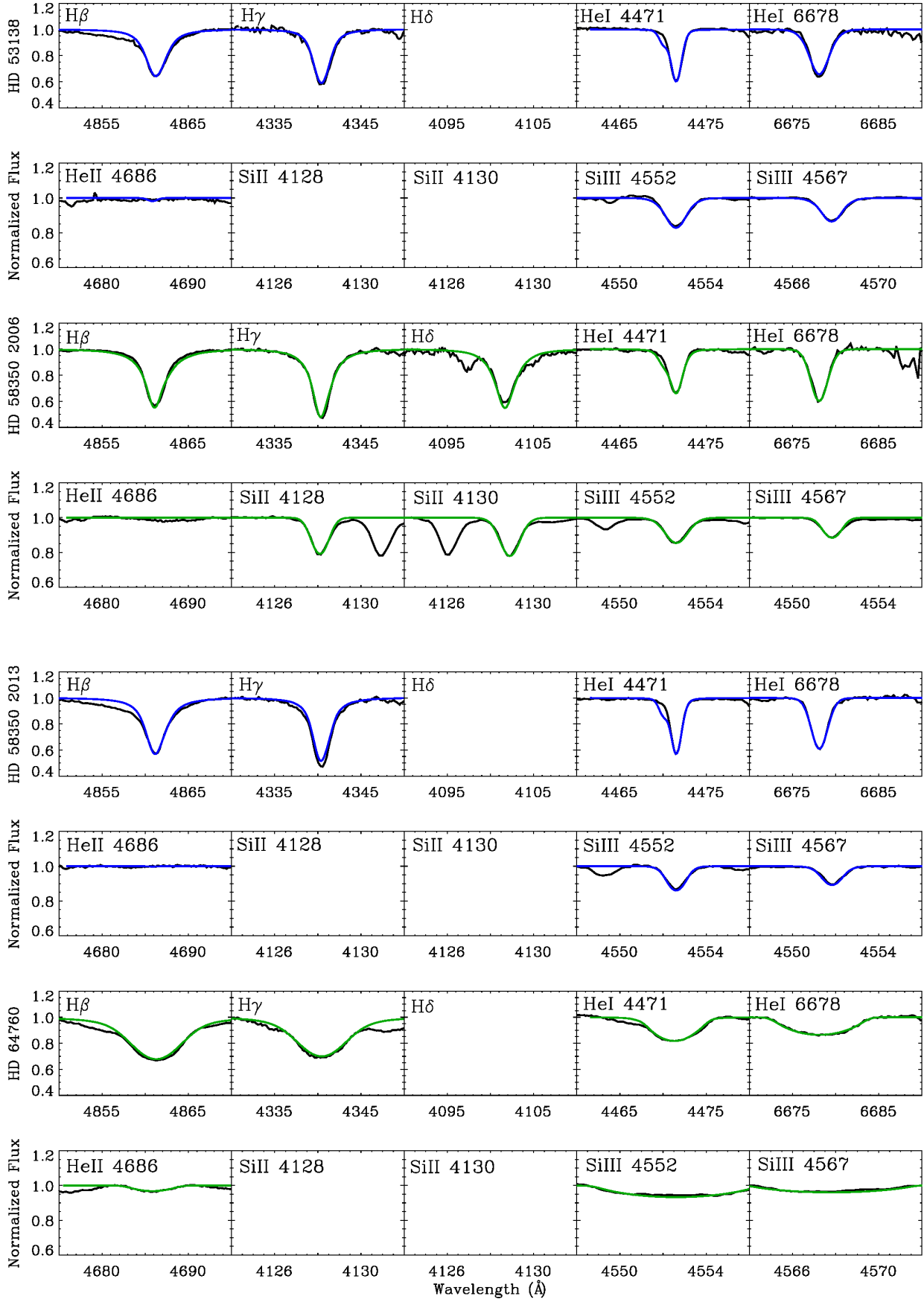


Fig. A.3. HD 53138, HD 58350, and HD 64760: Line model fittings to observations.

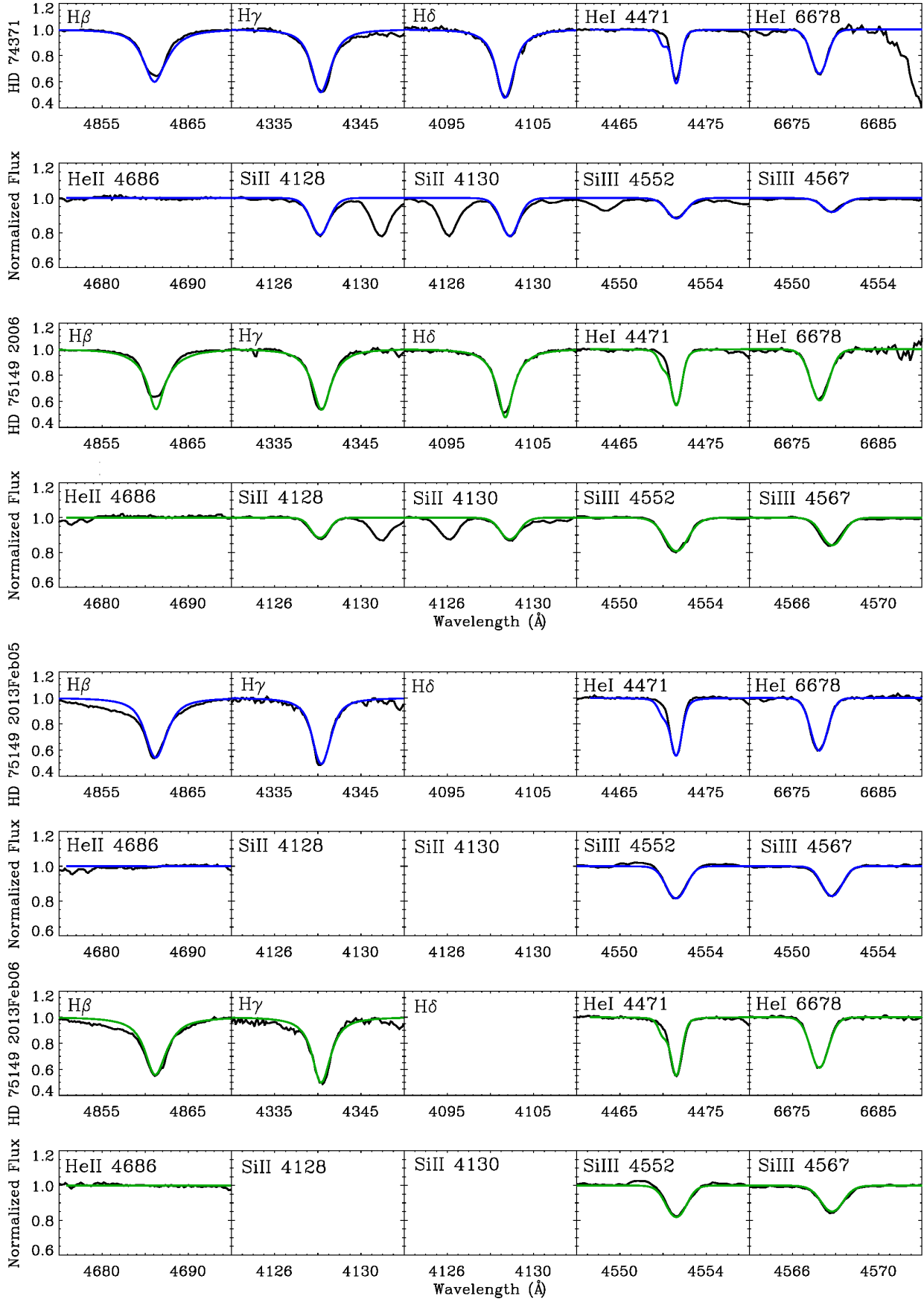


Fig. A.4. HD 74371 and HD 75149: Line model fittings to observations.

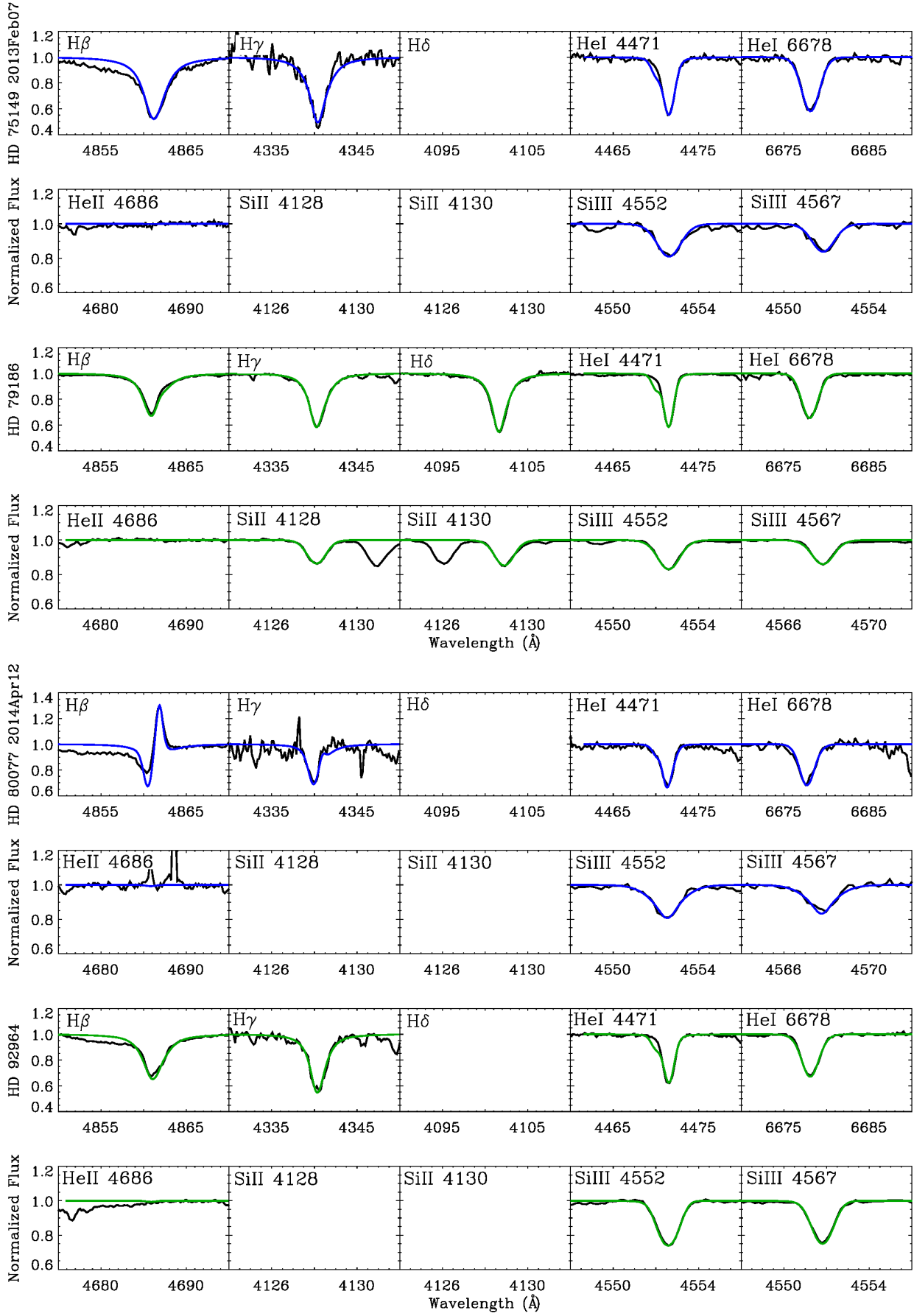


Fig. A.5. HD 75149, HD 79186, HD 92964, and HD 80077: Line model fittings to observations.

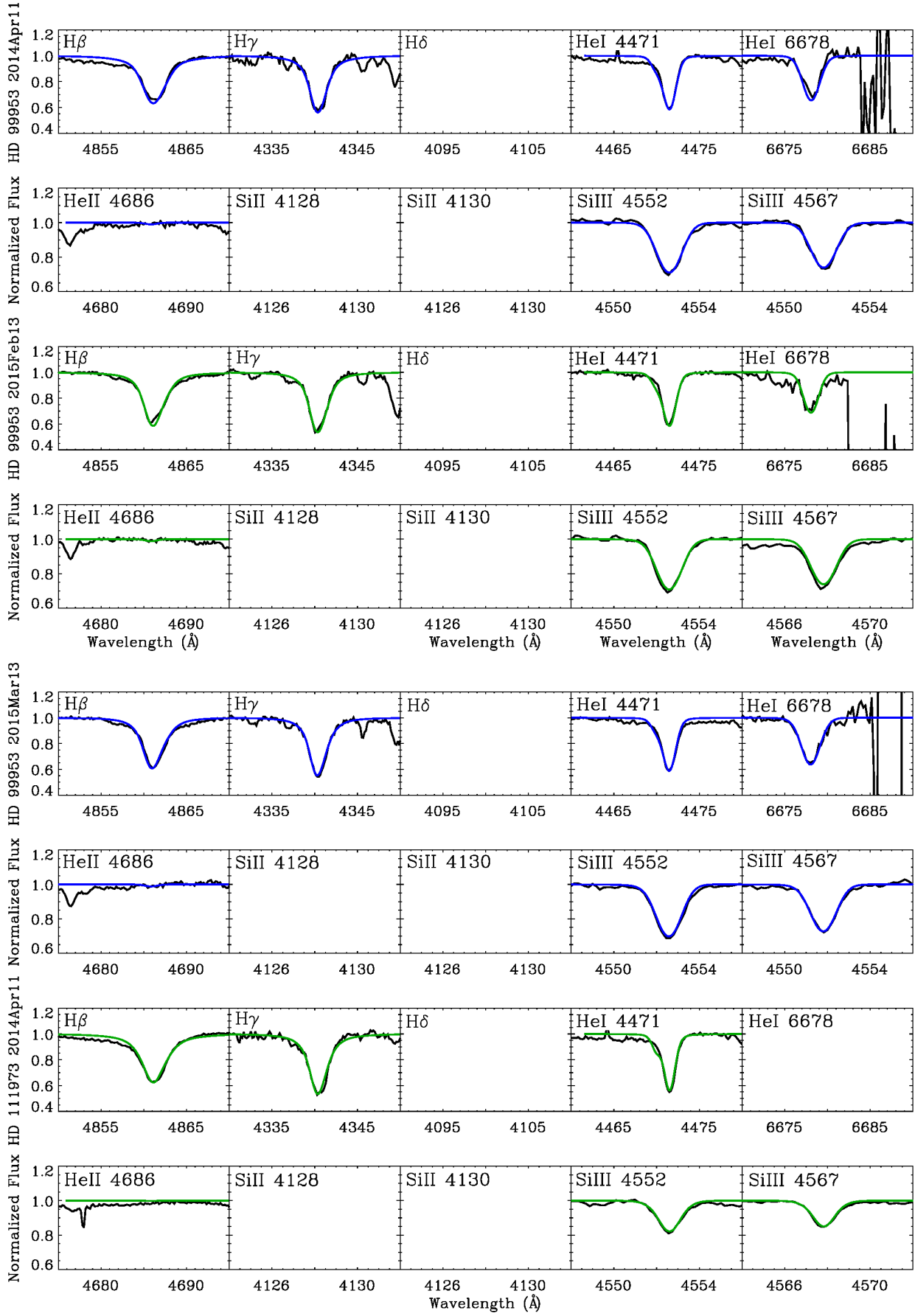


Fig. A.6. HD 99953 and HD 111973: Line model fittings to observations.

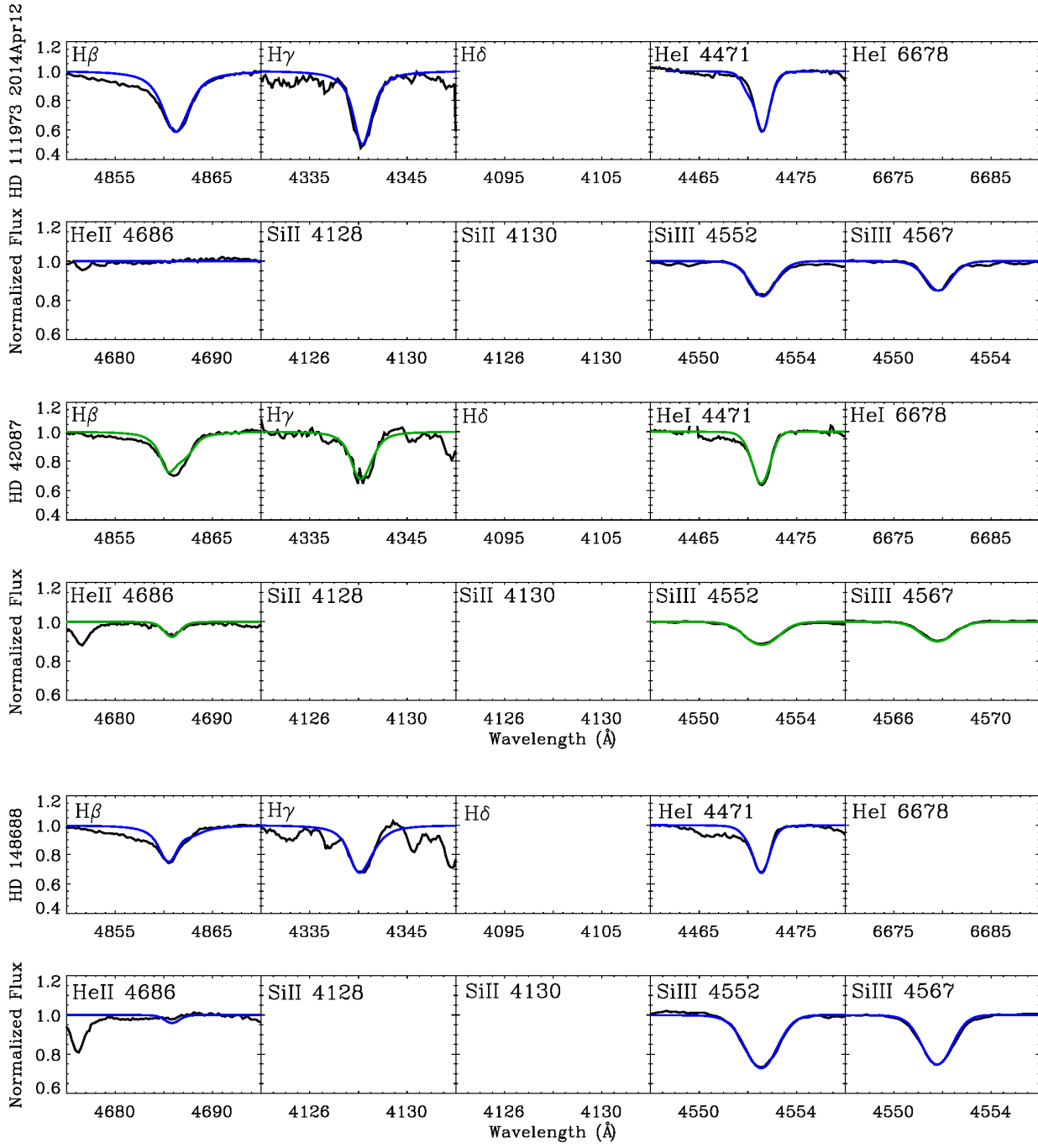


Fig. A.7. HD 111973, HD 115842, and HD 148688: Line model fittings to observations.